Microenvironment of metastatic site reveals key predictors of PD-1 blockade response in renal cell carcinoma

Florian Jeanneret[1], Pauline Bazelle[1#], Sarah Schoch[2#], Catherine Pillet[3], In Hwa Um[4], Assilah Bouzit[5], Bertrand Evrard[6], Evan Seffar[7], Frédéric Chalmel[6], Javier A Alfaro[8], Catia Pesquita[9], Fabio Massimo Zanzotto[10], Mark Stares[11,12], Stefan N Symeonides[11,12], Alexander Laird[13], Jean-Alexandre Long[5], Jean Luc Descotes[5], Delphine Pflieger[1], David J Harrison[4], Odile Filhol[3], Håkan Axelson[2], Christophe Battail[1]

[1] Univ. Grenoble Alpes, IRIG, Laboratoire Biosciences et Bioingénierie pour la Santé, UA 13 INSERM-CEA-UGA, CNRS FR 2048, 38000 Grenoble, France.

[2] Division of Translational Cancer Research, Department of Laboratory Medicine Lund University, Lund, Sweden.

[3] Univ. Grenoble Alpes, IRIG, Biosanté, UMR 1292 INSERM-CEA-UGA, 38000 Grenoble, France.

[4] School of Medicine, University of St Andrews, North Haugh, St Andrews KY16 9TF, Scotland, UK.

[5] Centre hospitalier universitaire Grenoble Alpes, CS 10217, 38043 Grenoble cedex 9, France.

[6] Inserm, EHESP, Irset (Institut de Recherche en Santé, Environnement et Travail), University Rennes, UMR_S 1085, F-35000 Rennes, France.

[7] Marie-Josée and Henry R. Kravis Center for Molecular Oncology, Memorial Sloan Kettering Cancer Center, New York, NY, USA. Department of Epidemiology and Biostatistics, Memorial Sloan Kettering Cancer Center, New York, NY, USA.

[8] International Centre for Cancer Vaccine Science, University of Gdansk, Gdansk, Poland.

[9] LASIGE, Faculdade de Ciências, Universidade de Lisboa, Lisboa, Portugal.

[10] Department of Enterprise Engineering, University of Rome "Tor Vergata", Rome, Italy.

[11] Edinburgh Cancer Centre, Western General Hospital, NHS Lothian, Edinburgh, UK.

[12] Institute of Genetics and Cancer, Cancer Research UK Edinburgh Centre, University of Edinburgh, Edinburgh, UK.

[13] Department of Urology, Western General Hospital, NHS Lothian, Edinburgh, UK.

# These authors contributed equally.

ABSTRACT

Immune checkpoint blockade (ICB) therapies have globally improved the overall survival (OS) of patients with advanced cancers. However, the response rate to these treatments vary widely among patients, therefore exposing non-responders to immune-related adverse events, causing an urgent need of prior-treatment predictors of response to ICB. We investigated the tumor microenvironment (TME) of clear cell renal cell carcinoma (ccRCC) samples from primary and metastatic sites to identify predictive molecular and cellular markers of response to ICB. We revealed a significant discrepancy in treatment response between TME subgroups inferred from metastatic sites. The C3 cluster was enriched in non-responders and harbored a lower fractions of T-CD8 and plasma B cells, as well as a decreased expression of immunoglobulin genes. In addition we developed a highly predictive score that reflects the Tumor-Immunity Differential (TID) in TME to predict immunotherapy response (AUC=0.88, log-rank tests for PFS $P < 0.0001$, OS $P = 0.01$). In addition, among TID-related genes (YWHAE, CXCR6 and BTF3), YWHAE was validated as a robust predictive marker of immunotherapy response in independent cohorts of melanoma and lung cancers based on pre or on-treatment biopsies. These findings provide insights into efficient ICB treatment selection in clinical practice for patients with advanced cancers.

INTRODUCTION

Immune checkpoint blockage (ICB) therapies have shown remarkable success in treating patients with advanced cancers by improving their recurrence rate and overall survival. However, only a subset of patients benefits from these therapies, and the response rate vary widely among patients and cancers (Hodi et al., 2010, Schadendorf et al., 2015, Robert et al., 2015, Braun et al., 2016, Motzer et al., 2018, Morad et al., 2021).

The lack of predictability of responders has led to the widespread use of first-line ICB therapies in more and more cancers, which can have significant patient side effects and costs on the healthcare system. To address this issue, it is essential to identify predictive biomarkers of response to ICB therapies to select patients who are most likely to benefit from these therapies and to avoid over-treatment in patients who are unlikely to respond.

Although recent analyses of histologic, genomic and various molecular features had furthered the understanding of the biological mechanisms underlying the response to ICB treatments, they have not provided highly predictive biomarkers (Braun et al., 2020, Wood et al., 2020, McGrail et al., 2021, Li et al., 2023).

To deliver the most suitable treatment to cancer patients, the development of predictive scores based on gene expression data has shown promising results in several cancer types including JAVELIN (Motzer et al., 2020-11) for ccRCC samples, or MIAS (Wu et al., 2022), GEP (Ayers et al., 2017), MHC-I and MHC-II (Liu et al., 2019), and IMPRES (Auslander et al, 2018) for melanoma samples. However, to our knowledge, none of these predictive scores is yet used in clinical practice (Lei 2021, Rosellini, 2023).

Moreover, the composition of the tumor microenvironment (TME) has been extensively described as a major component of the response to immunotherapies (Dieu-Nosjean, 2014, Germain et al., 2015, Fridman et al., 2017, Petitprez et al., 2020, Simonaggio et al., 2021).

In this work, we refine the analysis of recently published ccRCC single-cell data (Obradovic et al., 2021) to generate a comprehensive reference of ccRCC TME cell types from primary and metastatic sites, separately. We then exploite this reference by a cell deconvolution approach of bulk RNA-seq data to reveal new key cellular and molecular markers of the ICB treatment response and better understand their implications for ICB resistance. We identify three TME profiles associated with significantly different clinical responses to ICB therapy. In addition, we develop a score that reflects the Tumor-Immunity Differential (TID) in TME from metastatic samples of ccRCC which is highly predictive of treatment response to ICB treatments. Moreover, we identify TID-related genes and highlight YWHAE as an accurate predictor of ICB treatment response in ccRCC, melanoma and non-small cell lung cancer (NSCLC) based on pre or on-treatment biopsies.

MATERIAL AND METHODS

Public transcriptomics and clinical data

Processed bulk RNA-Seq and clinical data were collected for 5 different cohorts. A cohort of 331 primary and metastatic advanced clear cell Renal Cell Carcinoma (ccRCC) samples from patients that progressed on 1, 2 or 3 previous therapies (at least one systemic anti-angiogenic therapy) included in clinical trials CM-009 (NCT01358721), CM-010 (NCT01354431) and CM-025 (NCT01668784) treated by anti-PD-1 antibody Nivolumab and mTOR inhibitor Everolimus (EGAC00001001519; EGAC00001001520; EGAC00001001521) (Braun et al, 2020). A cohort of 11 primary or metastatic ccRCC samples on one of four clinical trials (NCT00441337, NCT00730639, NCT01354431, NCT01358721) processed in Wu et al., 2022 (Ascierto et al., 2016). A cohort of 64 advanced melanoma samples from patients included in clinical trial CA209-038 (NCT01621490) treated with Nivolumab (GSE91061) (Riaz et al, 2017). A cohort of 20 metastatic melanoma samples from patients treated by anti-PD-1 (GSE168204) (Du et al, 2021). A cohort of 19 peripheral CD8-T cells (PBMCs) samples collected from blood of metastatic NSCLC patients (GSE111414) (Trefny et al, 2019). Samples for each cohort were divided according to prior therapies and analyzed independently. Patients with treatment outcomes of “Complete Response” (CR) or Partial Response (PR) were considered as responders, whereas patients with treatment outcome of “Progressive Disease” (PD) as non-responders.

Single-cell RNA-seq data analysis

Single-cell RNA-seq data from 11 ccRCC patients was obtained from Obradovic *et al.* (Obradovic et al., 2021). Raw data was downloaded from https://data.mendeley.com/datasets/nc9bc8dn4m/1. The data set consisted of adjacent normal and tumor tissue. Both were analyzed separately. Furthermore, in the original study, the tissue was prior to sequencing FACS sorted into CD45+ and CD45- subsets. These subset annotations were kept, and the data were separately re-processed in R using Seurat (v.4.1.1) (Hao et al., 2021) and harmony (v.0.1.0) (Korsunsky et al., 2019). Initially,only features expressed in at least 50 cells were included in the analysis. Further QC included removal of cells with fewer than 200 and more than 5000 features detected. As kidney cells have in general a high mitochondrial content, its threshold was set to >25%, everything above was removed. To normalize the data, Seurat’s function NormalizeData was used followed by a feature selection to find the 2000 most variable genes. Afterward, the data was scaled by using the function ScaleData. Prior to data integration, a principal component analysis was carried out. To adjust for patient-to-patient variation, data integration was achieved by the function RunHarmony from the harmony package. For

dimensional reduction, uniform manifold approximation (UMAP) was performed on the first 20 dimensions of the harmony reductions. Finally, the Louvain algorithm implemented in Seurat was used for cluster analysis with a resolution of 0.5. To assign cell types to the clusters, differential gene expression (DGE) was used by applying Seurat's function FindAllMarkers. In addition to DGE, previously known cell type markers were used to facilitate cell type annotation.

To confirm the tumor origin of the annotated tumor cells, copy number variation (CNV) was inferred using the R package infercnv (v.1.12.0). As a normal reference the adjacent normal CD45- subset was used. The gene order file (hg38_gencode_v28.txt) was downloaded from https://data.broadinstitute.org/Trinity/CTAT/cnv/. For the analysis a gene cutoff of 0.1 was set. Furthermore, cluster_by_groups was set to TRUE and a noise filter was applied by setting sd_amplifier to 1.5. The hidden Markov model (HMM) i6 was used for CNV prediction.

Bulk RNA Barcoding (BRB) library preparation and sequencing

Total RNA was extracted from MCTS using the MirVana PARIS kit (Thermofisher). BRB-seq experiments were performed at the Research Institute for Environmental and Occupational Health (Irset, Rennes, France) according to the published protocol (Alpern et al, 2019). Briefly, the reverse transcription and the template switching reactions were performed using 4 µL total RNA at 2.5 ng/µL. RNA were first mixed with 1 µL barcoded oligo-dT (10 µM BU3 primers, Microsynth), 1 µL dNTP (desoxyribonucleoside triphosphate) (0.2 mM) in a PCR (Polymerase Chain Reaction) plate, incubated at 65 °C for 5 min and then put on ice. The first-strand synthesis reactions were performed in 10 µL total volume with 5 µL of RT (Reverse transcription) Buffer and 0.125 µL of Maxima H minus Reverse Transcriptase (Thermofisher Scientific) and 1 µL of 10 µM template switch oligo (TSO, IDT). The plates were then incubated at 42 °C for 90 min and then put on ice.

After reverse transcription (RT), decorated cDNA from multiple samples were pooled together and purified using the DNA Clean and concentrator-5 Kit (Zymo research). After elution with 20 µL of nuclease-free water, the samples were incubated with 1 µL Exonuclease I (NEB) and 2 µL of 10× reaction buffer at 37 °C for 30 min, followed by enzyme inactivation at 80 °C for 20 min.

Double-strand (ds) cDNAs were generated by PCR amplification in 50 µL total reaction volume using the Advantage 2 PCR Enzyme System (Clontech). PCR reaction was performed using 20 µL cDNA from the previous step, 5 µL of 10× Advantage 2 PCR buffer, 1 µL of dNTPs 50×, 1 µL of 10 µM LA-oligo (Microsynt), 1 µL of Advantage 2 Polymerase and 22 µL of nuclease-free water following the program (95 °C—1 min, 11 cycles: 95 °C—15 s, 65 °C—30 s, 68 °C—6 min, 72 °C—10 min). Full-length double-stranded cDNA was purified with 30 µL of AMPure XP magnetic beads (Beckman Coulter), eluted in 12 µL of nuclease-free water and quantified using the dsDNA QuantiFluor Dye System (Promega).

The sequencing libraries were built by tagmentation using 50 ng of ds cDNA with the Illumina Nextera XT Kit (Illumina) following the manufacturer's recommendations. The reaction was incubated for 5 min at 55 °C, immediately purified with DNA Clean and concentrator-5 Kit (Zymo research) and eluted with 21 µL of nuclease-free water. The tagmented library was PCR-amplified using 20 µL eluted cDNA, 2.5 µL of i7 Illumina Index, 2.5 µL of 5 µM P5-BRB primer (IDT) using the following program (72 °C—3 min, 98 °C—30 s, 13 cycles: 98 °C—10 s, 63 °C—30 s, 72 °C—5 min). The fragments ranging 300–800 base pairs (bp) were size-selected using SPRIselect (Beckman Coulter) (first round 0.65× beads, second 0.56×), with a final elution of 12 µL nuclease-free water. The resulting library was sequenced on an Illumina Hiseq 4000 sequencer as Paired-End 100 base reads following Illumina's instructions. Image

analysis and base calling were performed using RTA 2.7.7 and bcl2fastq 2.17.1.14. Adapter dimer reads were removed using DimerRemover (https://sourceforge.net/projects/dimerremover/).

BRB-seq data processing

Pair-end reads with quality score higher than 10 were kept. The first read of the pair is 16 bases long. A first part of 6 bases corresponds to a unique sample-specific barcode and a second part of 10 bp is a unique molecular identifier (UMI). The second read of the pair, containing genomic data, was aligned to the human reference transcriptome from the UCSC website (release hg38) using BWA (Li et al, 2009) (version 0.7.4.4) with the non-default parameter "–l 24". Reads mapping to several positions in the genome were filtered out from the analysis. The pipeline is described in Draskau et al (Draskau et al, 2021). After quality control and data pre-processing, a gene count matrix was generated by counting the number of unique UMIs associated with each gene for each sample.

Cell deconvolution algorithms

Prediction of tumor micro-environment (TME) cell type proportions from bulk gene gene expression data was performed using CIBERSORTx (version 1.0, 12/21/2019) and MuSiC (version 1.0.0) algorithms (Wang et al, 2019; Newman et al, 2019). The CIBERSORTx cell fractions module was executed using the docker image after registration and access token received (https://cibersortx.stanford.edu/download.php). For both methods, reprocessed and relabeled single-cell RNA-seq data were used as reference (Obradovic et al., 2021). The 3 tumor predicted fractions ("Tumor cells", "Cycling Tumor cells", "Tumor cells CA9-high") were summed into one "Tumor" fraction for clustering of samples based on estimated cell fractions.

Pseudo-bulk RNA-seq mixtures

The generation of a pseudo-bulk mixtures was performed from a single-cell RNA-seq data matrix made of several labeled cell types with gene expression in read counts. A step (1) consisted of sampling the single-cell RNA-seq data matrix. The number of cells of each cell type i used to construct the pseudo-bulk sample was defined using a random number R generated from Dirichlet's law multiplied by the number of cells S of that type i present in the single-cell RNA-seq data matrix.

$$N_i = R_i * S_i$$

A matrix M, corresponding to the cells belonging to a pseudo-bulk mixture, is therefore made up of N_i columns for each cell type i. A step (2) consisted in obtaining a pseudo-bulk sample by summing per gene the count values of reads across the cells of the different cell types. Steps (1) and (2) were repeated as many times as the number of pseudo-bulk samples to be generated.

The proportions of the different cell types composing each pseudo-bulk sample being known, the pseudo-bulk samples were used to evaluate the performance of the cell deconvolution algorithms. Comparisons between expected and predicted cell proportions were made using Spearman's correlation coefficient, Root Mean Square Error (RMSE) coefficient and linear regression slope.

Tumor purity analysis

A tumor purity score corresponds to the proportion of tumor cells in a sample. A tumor purity score was calculated for each sample from the gene expression values of its bulk transcriptome using the ESTIMATE method (Estimation of STromal and immune cells in MAlignant Tumor tissues using

Expression data) (Yoshihara et al., 2013). When available, the tumor purity score calculated from genomic profiling data of each tumor sample using the ABSOLUTE method (Carter et al, 2012) was also collected.

Tumor-Immunity Differential score

The Tumor-Immunity Differential (TID) score reflects the difference between tumor and immunity activities in samples. It was built from four predicted TME cell fractions (Tumor, CD8.T, Plasma and Treg cells) and genomic features (Tumor Mutation Burden (TMB) score, PDCD1 (PD-1) gene expression) frequently associated with patient response to ICB treatment. All features were standardized using Z-score transformation to make them comparable. The TID score was then defined as the difference between features considered unfavorable to the patient's response to treatment, tumor cell fraction and TMB score (For the Braun et al. 2020 cohort of metastatic samples, 11 missing TMB scores were inferred by the median value), and those considered favorable, PD-1 expression and for regulatory T cell, CD8+ T cell and Plasma cell fractions (Eq. 1). The status of each feature was inferred from their independent association with patient clinical benefit.

$$TID_{score} = \left(Tumor_{fraction} + TMB_{score}\right) - \left(PDCD1_{expression} + CD8\ T_{fraction} + Plasma_{fraction} + Treg_{fraction}\right)$$

Equation 1: calculation of the Tumor-Immunity Differential score

Therefore, the higher the TID score, the less favorable the patient's prognosis. High-TID and Low-TID sample categories were defined according to by the median value of the TID score distribution.

Clustering analysis

Unsupervised consensus clustering methods were implemented by the R/Bioconductor package ConsensusClusterPlus (version 1.62.0). Clustering of cell fractions and gene expression values were performed by k-means (parameters: reps = 1000, pItem = 0.8, pFeature = 1, clusterAlg = "km", distance = "euclidean"). The best number of clusters was assessed by the delta area plot of consensus Cumulative Density Function (CDF). To construct relevant groups of ccRCC samples in terms of treatment response we retained only cell fractions predicted by the CIBERTSORTx algorithm associated with clinical benefit (two-sided Wilcoxon rank-sum test, corrected p-value < 0.05 or corrected p-value < 0.20, for, respectively, metastatic tumor and others if no one fraction was selected by the first threshold). TME subtypes (C1-C3) of the 311 ccRCC samples with treatment response were found based on the consensus clustering of the selected cell fractions. Gene expression subtypes (G1-G4) were obtained by a consensus clustering of genes selected by a two-step process. Firstly, the differentially expressed genes between cluster of cells in single-cell RNA-Seq of ccRCC data (Obradovic et al., 2021) were selected for each cell type (corrected p-value < 0.05). Then, the 6 genes related to metastatic TME C1-C3 clusters were retained (two-sided Wilcoxon rank-sum test, corrected p-value < 0.05).

Statistical tests

Statistical differences of cell fraction or gene expression values for comparisons were assessed using two-sided Wilcoxon rank-sum test with the Benjamini-Hochberg correction for multiple hypothesis

testing. For sample comparisons across three or more groups, Kruskal-Wallis and two-sided chi-squared tests were used for numerical or categorical values, respectively.

Survival analysis

Survival analyzes were performed using the R package survival (version 3.4-0) . The Kaplan-Meier curves of Progression-Free Survival (PFS) and Overall Survival (OS) were used to compare prognosis. The statistical comparison of the survival outcomes between subtypes was done using the log-rank test from the R package survminer (version 0.4.9).

Gene ontology enrichment analysis

The R package clusterProfiler (version 4.6.0) was used to perform over-representation enrichment analysis of the 6 differentially expressed genes (DEG) between C1-C3 TME clusters based on the Gene Ontology (GO) Biological Process database.

Immunotherapy treatment outcome scores

Single-sample Gene Set Enrichment Analysis (ssGSEA) was used to compute the MHCI and MHCII prognostic scores based on previously published gene signatures (Liu et al., 2019). Gene Set Variation Analysis (GSVA) was used to compute the MIAS and GEP prognostic scores based on gene signatures previously reported (Wu et al., 2022, Ayers et al., 2017). The JAVELIN score was calculated as the average of the standardized values of the 26 genes within the 26-gene JAVELIN Renal 101 Immuno signature (Motzer et al., 2020-11). The IMPRES score was calculated from the method previously published (Auslander et al, 2018). The two Tertiary Lymphoid Structure (TLS) scores were computed based on the mean of a 9-gene signature (CD79B, EIF1AY, PTGDS, RBP5, SKAP1, LAT, CETP, CD1D, CCR6) (Cabrita et al., 2020) or a 7-gene signature (CCL19, CCL21, CXCL13, CCR7, CXCR5, SELL, LAMP3) (Dieu-Nosjean et al., 2014).

Immunofluorescence and histology image analysis

Formalin fixed paraffin embedded tissue blocks were sectioned at 5µm thickness. The tissue sections were dewaxed and rehydrated in xylene, gradual percentages of alcohols and finally in tap water. Protein epitopes of interest (CD8, particularly for CD8 positive lymphocytes, CD34 for endothelial cells equivalent to CD34, and CD45 for all leuckocytes) were retrieved in pH6 sodium citrate buffer using heat-induced epitope retrieval (HIER) method for 5 min, followed by quenching endogenous peroxidase activity and possible non-specific staining using 3% hydrogen peroxide (Sigma, H1009) and serum-free protein block (Agilent, X090930-2), respectively. Primary antibody - CD8 (Agilent, M710301-2, 1:800), and CD34 (Human Protein Atlas, HPA067440, 1:400), CD45 (Abcam, ab40763, 1:500) - was incubated for 1 hour at room temperature, followed by HRP (horseradish peroxidase) conjugated secondary antibody (Leica biosystems, DS9800) for 30 min. Fluorophore conjugated TSA (tyramide signal amplification) (Akoya bioscience, NEL744001KT, NEL741001KT) was used to visualize the primary antibody for 20 min. Then the sections were counterstained in Hoechst (Thermo fisher, H3570, 1:100) for 10 min and mounted in prolong gold anti-fade mountant (Thermo fisher, P36930). Zeiss axio scan z1 was utilized to acquire digitized images using fluorescence channels such as Hoechst, FITC and Cy3. Images were then analysed using HighPlex FL module in Halo AI (Indica Labs® version 3.6.4134) according to published protocol (Kaghazchi et al., 2022).

RESULTS

Extended labeling of ccRCC tumor micro-environment cells

A comprehensive literature review was performed to identify markers, mainly cell surface proteins, known to specifically label cell types present in the tumor micro-environment. This led us to construct a hierarchical decision tree summarizing the state of the art concerning associations between cell surface markers and identification of the different cell types present in the ccRCC micro-environment. Single-cell RNA-seq data generated from 11 treatment-naive resected ccRCC tumors were then collected from a previously published study (Obradovic et al., 2021). We completely reprocessed this dataset through pre-processing, quality control, normalization and cell clustering steps. In this study immune- and non-immune cells were separated by CD45-based fluorescence-activated cell sorting (FACS). We then relied on our hierarchical decision tree of cell surface markers to precisely label the different cell types present in this data set. Based on our reanalysis of the cells retrieved from all patients we could define 21 distinct cell types, including 3 tumor types (Tumor cells, CA9 High Tumor cells, Cycling Tumor cells) (Fig. 1A, B). We assessed these identifications by controlling gene expressions of all of the specific gene markers of immune and non-immune cells. In addition, the tumor cell populations were examined by the prediction of copy number variants (CNV). We observed that predicted tumor cells harbored a deletion of chromosome 3p region (VHL, PBRM1, BAP1, SET2D) and an amplification of the 5q region which is consistent with ccRCC (Chen et al., 2009, Peña-Llopis et al., 2013).

When pooling the cells from all patients we noticed that the tumor cell types constituted 35% of all cells (Fig. 1C). Regarding immune cell populations, monocytes constituted 15.2 %, NK cells 10.7%, CD4-T 9.9% and CD8-T 8.6% for a total of 51.4% for the complete immune cell population. These results are consistent with other single-cell analyzes of immune cell proportions from ccRCC tissue (Borcherding et al, 2021).

Robust prediction of ccRCC tumor micro-environment by cell deconvolution

Building on the work of extensive labeling of ccRCC cell populations and its cellular microenvironment, we assessed the relevance of using these single-cell RNA-seq data as reference profiles for cell deconvolution. Transcriptome-based cell deconvolution approaches make it possible to predict the respective proportions of cell types present in a tissue from its bulk transcriptome. We selected the CIBERSORTx and MuSiC methods (Wang et al, 2019, Newman et al, 2019), considered by recent benchmarks to be among the most accurate (Avila Cobos et al, 2020), and evaluated their ability to predict the respective proportions of the 21 cell types referenced in our single-cell data. To perform this evaluation, we generated test datasets corresponding to 100 pseudo-bulk mixtures by sampling and mixing in controlled and known proportions the reference single-cell RNA-seq profiles. In this way we avoid technical (i.e. different sequencing technology) or biological (i.e. same biological samples) bias between our test datasets and the reference single-cell data. We predicted the proportions of cell types for each pseudo-bulk mixture and assessed the robustness of the estimated fractions obtained by cell deconvolution by comparing them to the expected cell type fractions. We found high correlation values (Rho ranging from 0.57 to 0.99, two-sided Spearman correlation test p-value < 0.0001) between predicted and expected cell type proportions associated with low RMSE (Root Mean Squared Error) dispersion values (Fig. 2A). In addition, the analysis of the slope of the regression line by cell type

between predicted and expected proportions showed good linearity often close to 1, illustrating the quantitative accuracy of the predicted cell type fractions (Fig. 2A).

Next, we focused on further evaluating the proportions of tumor cells predicted by cell deconvolution using our reference single-cell RNA-seq profiles. To our knowledge, no study has yet been performed on the ability to predict tumor faction (i.e. tumor purity) of ccRCC by cell deconvolution. Indeed, prediction of tumor purity of tissues from genomic or transcriptomic data is frequently performed using the ABSOLUTE (Carter et al. 2012) and ESTIMATE (Yoshihara et al. 2013) algorithms, respectively. We compared tumor purity measures predicted by these different approaches using data from a previously published cohort of 311 ccRCCs (Braun et al, 2020). First, we predicted by cell deconvolution the proportions of the 21 cell types for each of the 311 transcriptomes. For the calculation of tumor purity, we summed the proportions of the 3 tumor cell types. Then, we used the ESTIMATE tool on these same 311 transcriptomes to predict a second tumor purity value. Finally, we collected from the supplementary data associated with the cohort a third tumor purity value generated by ABSOLUTE tool. We observed that the deconvolution-based estimated fractions of tumor cell were highly correlated to values predicted by ESTIMATE (two-sided Spearman correlation test p-value < 2.2e-16) (Fig. 2B) and ABSOLUTE (two-sided Spearman correlation test p-value=1.7e-11) (Fig. 2C). Moreover, the proportionality of the tumor purity predictions obtained by cell deconvolution and by ESTIMATE were very reproducible, illustrating the relevance of this new approach. The proportionality of tumor purities was less stringent between those obtained by cell deconvolution and those produced by ABSOLUTE. This was however expected given the quite weak level of correlation already observed between tumor purities predicted from transcriptomic and genomic data (add reference).

Finally, we extended our validation study of cell type fractions estimated by cell deconvolution using cell counts directly measured by immunofluorescence (IF) for a cohort of 19 ccRCC primary tissues. The ccRCC tissue cohort was profiled by Bulk RNA Barcoding (BRB)-seq to quantify gene expression and imaged by IF to directly enumerate populations of CD8-positive (CD8+), endothelial cells expressing CD34 (CD34+) and CD45-positive (CD45+) leukocytes in red (left panel), yellow (center panel) and green (right panel), respectively (Fig. 3A). (Fig. 3A). The bulk transcriptomic data of each sample was analyzed by cell deconvolution with CIBERTSORTx using the support of our 21 cell types single-cell reference data. To allow comparison between the cell counts obtained by IHC using the surface markers CD8, CD34 and CD45, we have grouped the cell types predicted by cell deconvolution according to the expected presence of these markers in the single-cell data set. The CD8-T cells, cycling T+NK cells and NK cells CD16+/FGFBP2+ were considered as CD8+ cells, the endothelial and Tip cells were selected as CD34+ cells and the DC, pDC, classical monocytes, intermediate monocytes, non-classical monocytes, B cells, plasma B cells, cycling T+NK, NK cells CD16-/FGFBP2-, NK cells CD16+/FGFBP2+, CD45-pos, T regulatory (T reg), CD4-T, CD8-T and mast cells were grouped as CD45+ cells. We therefore summed for each of the 19 samples the predicted cell fractions as described above in order to estimate the proportions of CD8+, CD34+ and CD45+ cells that we compared to the IHC measurements. We observed significant correlations between IHC-based quantification and CIBERSORTx-based estimation for the CD8+ and CD34+ cells (two-sided Spearman correlation test $P < 0.05$) (Fig. 3B left and center panels) and a positive trend for the CD45+ cells (two-sided Spearman correlation test $P = 0.075$) (Fig. 3B right panel). For each of these 3 populations, we finally extracted the respective contributions, predicted by cell deconvolution, of the cell types composing them. As expected, the CD8+ population was predicted to be predominantly composed of the CD8-T cell type (Fig. 3C left panel). The CD34+ population seemed to be constituted in a balanced manner by

endothelial and Tip cells (Fig. 3C center panel). As for the CD45+ population, cell deconvolution predictions seemed to reveal a composition in favor of the types DC, intermediate monocytes, B and NK cells (Fig. 3C right panel).

Micro-environment of ccRCC metastases predicts patient response to Nivolumab

The tumor micro-environment is increasingly considered to be a key factor to understand and attempt to predict the response of patients to anti-tumor treatments, in particular to immunotherapies (Dieu-Nosjean, 2014, Germain et al., 2015, Fridman et al., 2017, Petitprez et al., 2020). The cell deconvolution approach offers the possibility of analyzing the transcriptomic data of tumor tissue cohorts, from patients included in clinical drug trials, in order to reveal the content of their tumor micro-environments (TME). We validated, in the previous section, our cell deconvolution approach based on the CIBERTSORTx algorithm and single-cell reference transcriptomes for 21 cell types of the ccRCC micro-environment. We therefore used it to predict by deconvolution the cell fractions for each transcriptome of the 311 tumor samples from patients included in the clinical trials CheckMate of the anti-PD-1 antibody Nivolumab or mTOR inhibitor Everolimus in advanced ccRCCs (CM-009 (NCT01358721), CM-010 (NCT01354431) and CM-025 (NCT01668784)) (Braun et al., 2020). This cohort was selected because it is one of the few to be composed of samples obtained from the primary tumor site or from metastatic sites of patients associated with clinical metadata describing their responses to therapy (Clinical Benefit (CB), Progression Free Survival (PFS), Overall Survival (OS)).

First, to control putative gender-related bias, we estimated cell fractions for primary and metastatic tissues separately and did not find a significant difference in TME composition between men and women after correction for multiple testing. Next, regardless the gender, we subdivided the cohort into 4 subgroups based on sample collection site (primary/metastasis) and therapy followed by the patient (Everolimus/Nivolumab). The cell type proportions were then predicted by cell deconvolution for each subgroup. We first observed no statistical association between variations in TME and patient response to Everolimus from the subgroup of 92 primary tissues or of 37 metastasis. Next, we studied the subgroup of 133 primary tumor samples from patients treated with Nivolumab but also did not observe significant association between the TME composition and clinical variables of response to treatment or survival.

We finally selected among the 311 ccRCCs of the total cohort, the 84 tissues corresponding to metastases then further reduced our selection to the 47 samples taken before the treatment of patients with Nivolumab (Fig. 4A). We performed statistical associations analyzes between the cell fractions of each of the 19 cell types and the three categories of patient clinical benefit (Clinical Benefit (CB), Intermediate Clinical Benefit (ICB), Non-Clinical Benefit (NCB) defined by Braun et al. (Braun et al, 2020). Predicted cell fractions of Tumor, T regulatory, CD8-T and Plasma cells were significantly associated with CB or NCB responders before multiple testing procedure (two-sided Wilcoxon rank-sum test: p-value < 0.05, Fig. 4B). These four cell types identified as key populations of the ccRCC TME were kept for further analysis.

In order to reveal cell fraction profiles associated with patient clinical outcome to Nivolumab, we performed consensus clustering of k-means of the 47 metastatic ccRCC samples, based on Tumor, T regulatory, CD8-T and Plasma cell fractions, and classified them into three TME subtypes (C1-C3) (Fig. 4C). Among these subtypes, tumors in C1 showed better treatment response outcomes than tumors in C3 (two-sided chi-squared test p-value < 0.05), the latter being characterized by a high proportion

of poor response cases (NCB). The C2 subtype groups together a mixed population of patients with regard to their clinical benefit. We found that the tumor shrinkage values were significantly different between C1, C2 and C3 subtypes with mean values of -34, -6.4 and +16, respectively (Kruskal-Wallis test, p-value < 0.05). We finally performed survival analyzes and found that ccRCC tumors from C1 subtype harbored greater PFS (two-sided log-rank test p-value = 0.0066) indicating less post-treatment recurrence and greater OS (two-sided log-rank test p-value < 0.05) than C2-C3 sybtypes (Fig. 4E). As for metastatic sites, TMB counts, gene mutation profiles, tumor purity, sex and age, they were not different between these 3 subtypes (Kruskal-Wallis or two-sided chi-squared tests, p-value > 0.05)

Regarding the TME content, the C1 subtype was associated with a higher fraction of CD8 T-cells and of plasma cells compared to C2-C3 and C3, respectively (Fig. 4D). Plasma cells were able to distinguish the mixed C2 subtype from the C3 subtype of poor responders, the latter being associated with significantly lower fractions. (Fig. 4D). These results were consistent with the presence of Tertiary Lymphoïd Structures (TLS) in the tumor that were highlighted as key actors for sustaining an immune-responsive micro-environment (Dieu-Nosjean et al., 2014, Cabrita et al., 2020, Helmink et al., 2020). The TLS status were calculated by dividing the Braun et al. 2020 cohort of 47 metastatic ccRCC samples by the median values of TLS scores derived from 2 gene signatures (Dieu-Nosjean et al., 2014, Cabrita et al., 2020). We observed that the C1 subtype was enriched in TLS-High status compared to the C3 subtype (Fig. 4C).

To further characterize the mechanisms contributing to the differences of patient response outcomes between C1, C2 and C3 TME subtypes, we used gene signature previously identified as correlated with angiogenesis (Angio) (McDermott et al., 2018), myeloid cell infiltration (Myeloid) (McDermott et al., 2018), T effector cell infiltration (Teff) (McDermott et al., 2018), Tumor Inflammation Score (TIS) (Danaher et al., 2018), and immune infiltration (JAVELIN) (Motzer et al., 2020, Braun et al., 2020). We observed that C1 subtype tumors were associated with greater Teff, JAVELIN and TIS scores, compared to C3, C2-C3 and C3 respectively (two-sided Wilcoxon rank-sum test, Benjamini-Hochberg-corrected p-value < 0.05, p-value < 0.01 and p-value < 0.01) (Fig. 4F). These results confirmed the high immune infiltration, in particular in T cells, of C1 subtype in parallel with strong angiogenesis allowing immune cells to reach tumor cells, biological features known to promote the beneficial response of patients to immunotherapies (McDermott et al., 2018, Danaher et al., 2018, Motzer et al., 2020).

Immunoglobulin gene signature from ccRCC metastases predicts patient response to Nivolumab

The exploration of the micro-environment of ccRCC metastases continued with the aim of revealing a gene signature capable of reproducing the predictive characteristics identified in the previous section, while facilitating translation into the clinic. We leveraged the reprocessed and relabeled single-cell RNA-seq data of the ccRCC and performed pair-wise comparisons between cell-type transcriptomes to identify sets of differentially expressed genes specific to each cell type (Fig. 5A). Then, only the gene sets of the 4 cell types previously identified as associated with the response of patients to Nivolumab (Tumor, T regulatory, CD8-T and Plasma cells) were considered. Finally, we reduced the list of genes to those significantly differentially expressed between the C1, C2 or C3 cell-based subtypes (two-sided Wilcoxon rank-sum test, Benjamini-Hochberg-corrected p-value < 0.05) (Fig. 5B). Interestingly, this gene selection process revealed 6 genes: *TMEM139*, whose reduced expression is associated with a poor prognosis in Non-Small Cell Lung Cancer (NSCLC) (Zhang et al, 2022) and 5 immunoglobulin genes coding for the constant region of immunoglobulin light chains (*IGKC*) and heavy chains (*IGHG1*, *IGHG2*,

IGHG3, *IGHA1*). As expected, analysis of this 6-gene signature by functional enrichment of biological processes (GO) indicated its involvement in the tumoral immune response mediated by B cells.

We then assessed the ability of this 6-gene signature to classify the cohort of 47 ccRCC metastases using a consensus clustering based on k-means (Fig. 5C). This analysis led to the identification of 4-gene-based subtypes (G1–G4), with a G1 cluster enriched in patient with good clinical benefit (CB) and with G2, G3 and G4 clusters enriched in bad responders (NCB). Patients from G1 gene-based cluster had a better PFS than those classified in the other subtypes (Fig. 5D), while no significant difference OS was detected (Fig. 5E). The tumor shrinkage was associated with the gene-based cluster membership with the G1 and the G2 groups harboring, respectively, the best (-21) and the worst (+20) averaged values. As TMB counts, tumor purity, sex and age, were not significantly associated with gene-based subtypes (Kruskal-Wallis test, p-value > 0.05).

Interestingly, the G2 gene-based cluster was associated with a reduced expression of the 6-gene signature, compared to the other clusters. This result was highly consistent with C3 TME-subtype characterized by significantly low fractions of CD8 T and plasma cells and by a TLS-Low status (Fig. 5C, S2A). These results led to a consistent interpretation of this G2 gene-based subtype of poor prognosis to Nivolumab as depleted in immune infiltrate and particularly in antigen-secreting plasma cells involved in the humoral immune response. Interestingly, the G4 gene-based cluster of poor responders had the greatest expression of immunoglobulin genes, more than the G1 cluster of good responders (two-sided Wilcoxon rank-sum test, p-value < 0.05, Fig. 5C). In fact, the NCB responders in G4 were part of the C2 TME-subtype with mixed responses. This G4 cluster was characterized by a similar fraction of plasma cells as G1 but by a lower fraction of CD8 T cells. These results suggested that the expression of immunoglobulin genes and the proportions of plasma and CD8 T cells present in ccRCC metastases would be key determinants in predicting patient response to Nivolumab.

Tumor-Immunity Differential score predicts patient response to Nivolumab from ccRCC metastases

Leveraging on our results, we found that a wide variety of molecular and cellular properties of ccRCC metastases help classify patients based on their response to Nivolumab. In order to integrate these components, we developed a Tumor-Immunity Differential (TID) score that consisted of the difference between a tumor part of high predictive value for patients with NCB (Tumor cell fraction and TMB) and an immunity part of high predictive value for patients with good clinical benefit (CB) (Plasma B, CD8-T and Tref cell fractions and the *PDCD1* gene expression) (Fig. 6A and 6B). Therefore, the higher the TID score the worse the patient's prognosis should be. To assess this hypothesis, the cohort of 47 ccRCC metastases was divided using the TID score median value (0.78) resulting in 24 tumors with TID-Low status and 23 tumors with TID-High status. The TID-High subtype had indeed significantly worse clinical prognostic values and was enriched in patients with NCB responses for 15 out 23 tumors (1 CB, 7 ICB) whereas the TID-Low subtype was enriched in patients with CB responses for 12 out of 24 tumors (5 NCB, 7 ICB) (two-sided chi-squared test, p-value < 0.001) (Fig. 6C). Furthermore, the TID subtypes were significantly associated with patient PFS and OS (two-sided log-rank test, PFS: p-value < 1e−04 and OS: p-value = 0.01) (Fig. 6E and 6F). The TID-Low subtype of good prognostic also harbored lower tumor purity (ABSOLUTE value 0.28 vs. 0.39) and higher JAVELIN and TIS scores compared to TID-High subtype (two-sided Wilcoxon rank-sum test, Benjamini-Hochberg-corrected p-value < 0.05), highlighting for the latter a higher tumor content associated with a reduced tumor immune infiltrate (Fig. 6D).

We continued our investigation of TID subtypes by identifying genes whose expression significantly differed between these two groups. The *CXCR6* gene was under-expressed in TID-Low cluster, while the *YWHAE* and *BTF3* genes were over-expressed in TID-High subtype, the one associated with bad patient treatment outcome and poorer OS (two-sided Wilcoxon rank-sum test, Benjamini-Hochberg-corrected p-value < 0.05) (Fig. 6G).

Since the TID score integrates several molecular and cellular components that can be complicated to obtain in clinical routine, we studied the ability of this 3-gene signature to classify the cohort of 47 ccRCC metastases, using consensus clustering based on k-means, into TID-associated clusters TID-G1 and TID-G2 (Fig. 6H). These clusters were significantly associated with PFS,OS values and RECIST treatment outcomes with the TID-G1 showing a better treatment outcome and OS than TID-G2 (two-sided log-rank test, PFS: p-value = 1e−04, OS: p-value < 0.05) (Fig. 6I and 6J). Interestingly, *CXCR6* had higher expressed in TID-G1, compared to TID-G2, and associated with higher proportion of T-CD8 and plasma B cells, higher expression of immunoglobulin genes, and higher TLS scores (Fig. 6H). These results showed that the 3-gene signature allowed capturing the predictive power of the TID score from ccRCC metastases.

TID-associated *YWHAE* gene predicts patient response to Immune Checkpoint Blockade in melanoma and lung cancers

To assess the pan-cancer predictive power of the TID score and TID-associated genes (*CXCR6*, *YWHAE* and *BTF3*), we performed a comprehensive comparison of Immune Checkpoint Blockade (ICB)-response predictive scores previously published on additional cohorts of primary and metastatic cancer tissues from patients treated by anti-PD-1 or anti-CTLA-4 therapies. The ICB-related scores considered were transcriptomic-based predictive signatures, including JAVELIN (Motzer et al., 2020-11), MIAS (Wu et al., 2022), GEP (Ayers et al., 2017), MHC-I (Liu et al., 2019), MHC-II (Liu et al., 2019), IMPRES (Auslander et al, 2018), 2 TLS scores (TLS2014 (Dieu-Nosjean et al., 2014) and TLS2020 (Cabrita et al., 2020)), and the PD-1 gene (*PDCD1*) expression.

We initiated our comparison from cohorts of ccRCC tumor tissues obtained from patients before treatment with anti-PD1. The panel of scores predicting patient response to ICB were evaluated on 3 cohorts from two different studies: a first of 33 metastases (Braun et al, 2020), a second of 90 primary tumors (Braun et al, 2020) and a third of 9 primary tumors (Ascierto et al., 2016) (Fig. 7A). We found that the TID score was the best performing predictor of anti-PD1 response in ccRCC metastases (AUC-ROC of 0.88), followed by MHCI and MHCII scores (AUC-ROC of 0.8 and 0.78) (Fig. 7A first plot). We also observed good performances for the 3 TID-associated genes (AUC-ROCs ranging from 0.73 to 0.76). Surprisingly, all of ICB response scores calculated with primary ccRCC samples or primary and metastatic samples from the Braun et al. 2020 and Ascierto et al. 2016 datasets obtained poor performances close to chance (AUC-ROCs ranging from 0.5 to 0.75) excepting for the *YWHAE* gene and IMPRESS score with AUC-ROCs of 0.75 (Fig. 7A third and fourth plots). To explain the discrepancy between the score performances for the ccRCC datasets, we assessed the correlations between both types of samples. We used an independent cohort of 15 matched primary and metastatic ccRCC samples (Ho et al., 2017) and calculated the same scores based on RNA gene expression data. We observed correlations between primary-based and metastatic-based scores for only poor performers: IG, IMPRES and TLS2020 scores (two-sided Spearman correlation test p-value < 0.05) (Fig. 7B) suggesting that treatment response prediction based on gene expressions in ccRCC is not correlated between primary and metastasis samples from the same patient.

To further validate the value of TID-associated genes beyond ccRCC, we investigated their ability of to predict the response to immunotherapies of patients with metastatic melanoma or metastatic non-small cell lung cancer (NSCLC), compared to published ICB response scores. More specifically, we used 2 cohorts of patients with metastatic melanoma treated with Nivolumab: a first one of 64 primary samples from Riaz et al. (Riaz et al. 2017) and a second one of 20 primary samples from Du et al. (Du et al. 2021). We also used a cohort from Trefny et al. (Trefny et al, 2019) of 19 blood samples with peripheral blood mononuclear cells (PBMCs, CD8-T cells) collected from patients with metastatic NSCLC treated with Nivolumab. These three studies having collected samples before and during treatment, we took advantage of their experimental design by dividing each cohort according to the time of the biopsy, into pre- and on-treatment samples (Fig. 7C and 7D). Furthermore, to assess how prior therapy could affect patient response to ICB, we divided the Riaz et al. 2017 cohort into groups of patients who had previously been treated with Ipilimumab (anti-CTLA-4) (31 samples) and those naive for this treatment (33 samples). Of note, less than 2 IG-genes out of 5 having been detected in melanoma and NSCLC transcriptomic datasets, they could not be used to assess the prediction of the IG signature.

Interestingly, for pre-treatment melanoma samples, the TID-associated *YWHAE* gene expression greatly outperformed the existing ICB response scores for the Ipilimumab-naive patients (AUC-ROC of 0.78) (Fig. 7C first plot) or was the best performer, with the MIAS score, for the patients who progressed after Ipilimumab (AUC-ROC of 0.89) (Fig. 7C second plot), and was among the top predictors in the Du et al. cohort (AUC-ROC of 0.94) (Fig. 7C third plot). Regarding PBMCs samples from the Trefny et al. 2019 dataset, the expression levels of *YWHAE* and *PDCD1* genes were the best performers (AUC-ROC of 0.84) (Fig. 7C fourth plot). The average AUC-ROC values highlighted the YWHAE gene as the best marker of ICB treatment response based on pre-treatment biopsies (AUC-ROC of 0.85) (Fig. 7C fifth plot).

We continued our investigation of patients with melanoma or NSCLC using samples obtained during their treatment with Nivolumab. For the Riaz et al. 2017 melanoma cohort, we observed an overall improvement in the performance of the ICB response scores for the Ipilimumab-naive samples compared to those obtained from the biopsies taken before Nivolumab treatment (Fig. 7C and 7D first plots). The best predictive power was obtained by far with the *YWHAE* gene for Ipilimumab-naive samples from the Riaz et al. 2017 dataset (AUC-ROC of 0.98) (Fig. 7D first plot) and for that of Du et al. (AUC-ROC of 1) (Fig. 7D third plot). Regarding the melanoma samples from Riaz et al. 2017 taken from patients who progressed after treatment with Ipilimumab, we observed, unlike the Ipilimumab-naive patients, rather an overall reduction in the quality of the predictions with a performance for *YWHAE* (AUC-ROC of 0.73) slightly below that of the MIAS score (AUC-ROC of 0.8) (Fig. 7D second plot). Finally, for Trefny et al. PBMCs samples from the blood of patients with NSCLC, the performances of the ICB response scores were closed to those obtained from the samples taken from the patients before treatment (Fig 7D fourth plot). The *YWHAE* gene obtained the second best prediction (AUC-ROC of 0.75), just after that of the GEP score (AUC-ROC of 0.8), with a strong decrease in the performance of PDCD1. Overall, the average AUC-ROCs highlighted the *YWHAE* gene as the best marker of ICB response based on on-treatment biopsies (AUC-ROC of 0.86) (Fig. 7D fifth plot).

DISCUSSION

Immune checkpoint blockade (ICB) therapies are now a important tool in the arsenal for the treatment of advanced cancer with prolonged progression-free survival and overall survival (Hodi et al., 2010, Schadendorf et al., 2015, Motzer et al., 2018). However, only a subset of patients respond to ICB therapies causing an urgent need for novel approaches to better select patients who may benefit from these treatments (Schadendorf et al., 2015, Braun et al., 2016). Previous studies have shown the influence of the cellular composition of the tumor microenvironment (TME) on the response of patients to immunotherapies (Şenbabaoğlu et al, 2016; Lin et al, 2020; Bagaev et al, 2021; Ke et al, 2022). Although substantial effort has been devoted to the investigation of T cells populations in ICB treatment response understanding, other cell types in the TME are also involved in patient clinical outcome (Fridman et al., 2017; Petitprez et al., 2020).

Predicting the composition of the TME from bulk RNA-seq data by cell deconvolution approaches, especially those able to use single-cell RNA-seq data of cell types of interest as a reference, have proven to be robust and sensitive approaches (Avila Cobos et al, 2020). Since the quality of single-cell transcriptome labeling used as a reference of these methods has a major impact on the predictive performance, we carried out a detailed bibliographic study to identify markers allowing to annotate the cell types expected in the ccRCC. We then evaluated markers and combinations of markers on single-cell RNA-seq data from ccRCC tissues and selected the most resolving ones resulting in the annotation of 21 cell types (Obradovic et al., 2021). This annotated single-cell dataset was then used as a reference to perform cell deconvolution by CIBERTSORTx on bulk transcriptomic data of advanced ccRCC samples from primary and metastatic sites collected from patients before ICB treatment (Braun et al, 2020).

We further explored cell type proportions predicted on the cohort of ccRCC samples from Braun et al., 2020 and found that the tumor, Plasma B, CD8-T and T-regulatory cells fractions from metastases were highly valuable to identify several TME subtypes (C1-C3) with significant differences in anti-PD-1 treatment response, cancer progression and overall survival. By contrast, we observed no association between predicted TME and treatment response for samples from primary sites or for primary and metastatic samples treated by TKI (Everolimus). Moreover, differentially expressed genes between C1-C3 TME subtypes revealed 5 immunoglobulin genes (*IGKC*, *IGHG1*, *IGHG2*, *IGHG3*, *IGHA1*) as markers of the C3 TME cluster showing the worst ICB clinical response. This cluster is characterized by low expression of immunoglobulin genes and poor fractions of Plasma B cells showing the key role of Plasma-B cell in the anti-tumor immune response. This need of both B-cell and T-cell fractions for efficient immunotherapy treatment response is consistent with previous works in colorectal (Bindea et al., 2013), breast (Schmidt et al., 2008), NSCLC (Lohr et al., 2013), head and neck (van Herpen et al., 2008), and ovarian (Zhang et al., 2003) cancers where higher proportion of T-cells or B-cells in TME were associated to improved patient survival.

Besides, previous studies found that B cells associated with tertiary lymphoid structures (TLS) were involved in adaptive immune responses in inflamed and tumor tissues (Dieu-Nosjean et al., 2014, Germain et al., 2015, Cabrita et al., 2020). These ectopic lymphoid formations lead to the differentiation of key immune cells: tumor-specific B-cells acting either as antigen-presenting cells or tumor antigen-specific antibody-secreting cells and T-cells (Aloisi et al., 2006, Drayton et al., 2006). In recent works, TLS were also associated with ICB treatment responses in ccRCC and melanoma with a focus on TLS-associated B cells and gene signatures (Dieu-Nosjean et al., 2014, Cabrita et al., 2020,

Helmink et al., 2020). This is consistent with our results obtained using ccRCC metastases from the CheckMate cohorts (Braun et al. 2020), where high levels of CD8-T cells and Plasma B-cells fractions were correlated with the two TLS signatures. Furthermore, the TME-subtype C1 related to a high proportion of ICB responders being enriched in both CD8-T and Plasma B-cells TME fractions highlights the important interplay between these cell types that may occurs in TLS, especially in metastasis sites of patients with ccRCC.

In addition, we developed a single-sample Tumor-Immunity Differential (TID) score to leverage gene expression data and estimated TME cell fractions to cluster metastatic ccRCC samples. We based our score on both favorable (PDCD1 (PD-1) gene expression, T regulatory, CD8-T and Plasma cell fractions) and unfavorable (Tumor and TMB) features for ICB response. The TID score is then calculated as the difference between the ICB response unfavorable "tumor" and the favorable "immunity" parts. We observed that the TID-High subtype was strongly correlated with bad responders, recurrence and with a poorer overall survival. Also, high TMB values appeared as associated with bad ICB response in metastatic ccRCC samples. This observation is directly linked with recent works in ccRCC that have shown that high TMB values were associated with poor survival and immune infiltration (Zhang et al., 2019) and with a limited predictive clinical value of ICB response (Wood et al., 2020, McGrail et al., 2021). Moreover, a high tumor purity was found in the High-TID subtype of bad ICB responder, suggesting that tumor fraction or purity were a key component driving ICB treatment response in metastatic ccRCC samples. Moreover, three genes were highlighted as markers of the TID subtypes: *YWHAE*, *CXCR6* and *BTF3*. The *YWHAE* gene belongs to the 14-3-3 protein family and was previously found to be associated with advanced ovarian cancers, and poor patient prognosis mediated by the PI3K/AKT and MAPK pathways (Li et al., 2021). Interestingly, phenethyl isothiocyanate (PEITC) and fusicoccin molecules are found in the DrugBank database to target 14-3-3 proteins. Previous studies revealed various anti-cancer effects of PEITC molecules (Gupta et al., 2014), leading to an inhibition of carcinogen metabolism in smokers with lung cancer (Yuan et al., 2016) while Fusicoccin-A induces apoptosis in human cancer cell lines in combination with or after IFN-α treatment (de Vries-van Leeuwen et al., 2010, Andlovic et al., 2023). *CXCR6* is a chemokine receptor overexpressed in tumour-infiltrating lymphocytes involved in the recruitment of T cells into RCC tissue (Oldham et al., 2012). The Basic Transcription Factor 3 (*BTF3*) is required for the transcriptional initiation and known to be an oncogene in colorectal cancer (Wang et al., 2021), overexpressed in pancreatic ductal carcinoma cells (Kusumawidjaja et al., 2007) and in prostate cancer where it sustains cancer stem-like phenotype (Symes et al., 2013, Hu et al., 2019). To further assess the clinical relevance of the TID score and the associated genes, we compared them to existing transcriptomic scores previously published to predict patient clinical response to ICB therapy. We observed that the TID score was the best predictor of patient clinical benefit on the cohort of metastatic ccRCC samples from the CheckMate cohorts (Braun et al. 2020).

In order to assess the predictive power of marker genes associated with the TID score, we extended comparisons of scores and markers predicting ICB clinical response to melanoma and NSCLC cancers. The classification performances of the TID-associated *YWHAE* gene outperformed other existing scores in anti-PD-1 treated metastatic melanoma and NSCLC cancers in pre-treatment and on-treatment samples. Notably, the best performances in the NSCLC Trefny et al. 2019 subgroups were obtained using gene expressions of *YWHAE* and *PDCD1* although the analyzed samples were peripheral blood circulating CD8-T cells. These results reinforced the clinical relevance of peripheral CD8-T cells in the prediction of ICB response in NSCLC and suggested a novel key role in cancer for *YWHAE* in CD8-T cells.

Interestingly, the investigation of a variety of tumor sample types with different biopsy time-points (pre or post-treatment by anti-PD-1 antibody) from several cohorts revealed the discrepancy in the treatment outcome prediction performance of predictive scores based on gene expression data. We observed poorer performances for samples from the primary site of ccRCC compared to the samples from one metastatic site (CheckMate cohorts) with no correlation between both types of samples between scores calculated on matched primary and metastatic sites (Ho et al. dataset). Also, the prediction performances were not equivalent between pre or post-treatment samples or samples recruited or not after the failure of one previous anti-CTLA-4 immunotherapy in melanoma samples which is consistent with a previous study on patients with melanoma treated with Nivolumab or Pembrolizumab showing that previous anti-CTLA-4 exposure was associated with performance differences for treatment outcome prediction (Liu et al., 2019).

To conclude, we highlighted in this work the importance of the interplay of both CD8-T and Plasma B cells in immunotherapy response in ccRCC and we revealed the 5 immunoglobulin genes (*IGKC*, *IGHG1*, *IGHG2*, *IGHG3*, *IGHA1*), the Tumor-Immunity Differential score and the TID-associated genes *YWHAE* as powerful markers of ICB treatment response based on pre-treatment or on-treatment biopsies of primary sites, metastatic or peripheral CD8-T cells samples in several cancer types. Further validation studies in larger cohorts will be needed to finely assess the pan-cancer predictive performance and robustness of the TID score and of the key TID-associated gene markers. Our results open novel avenues to better predict the clinical outcome of patients with cancers treated by immunotherapies.

REFERENCES

Andlovic, B., Heilmann, G., Ninck, S., Andrei, S. A., Centorrino, F., Higuchi, Y., Kato, N., Brunsveld, L., Arkin, M., Menninger, S., Choidas, A., Wolf, A., Klebl, B., Kaschani, F., Kaiser, M., Eickhoff, J., & Ottmann, C. (2023). IFNα primes cancer cells for Fusicoccin-induced cell death via 14-3-3 PPI stabilization. Cell Chemical Biology, 30(6), 573-590.e6. https://doi.org/10.1016/j.chembiol.2023.04.005

Aloisi, F., & Pujol-Borrell, R. (2006). Lymphoid neogenesis in chronic inflammatory diseases. Nature reviews. Immunology, 6(3), 205–217. https://doi.org/10.1038/nri1786

Alpern, D., Gardeux, V., Russeil, J., Mangeat, B., Meireles-Filho, A. C. A., Breysse, R., Hacker, D., & Deplancke, B. (2019). BRB-seq: ultra-affordable high-throughput transcriptomics enabled by bulk RNA barcoding and sequencing. Genome biology, 20(1), 71. https://doi.org/10.1186/s13059-019-1671-x

Auslander, N., Zhang, G., Lee, J. S., Frederick, D. T., Miao, B., Moll, T., Tian, T., Wei, Z., Madan, S., Sullivan, R. J., Boland, G., Flaherty, K., Herlyn, M., & Ruppin, E. (2018). Robust prediction of response to immune checkpoint blockade therapy in metastatic melanoma. Nature medicine, 24(10), 1545–1549. https://doi.org/10.1038/s41591-018-0157-9

Avila Cobos, F., Alquicira-Hernandez, J., Powell, J. E., Mestdagh, P., & De Preter, K. (2020). Benchmarking of cell type deconvolution pipelines for transcriptomics data. Nature communications, 11(1), 5650. https://doi.org/10.1038/s41467-020-19015-1

Ayers, M., Lunceford, J., Nebozhyn, M., Murphy, E., Loboda, A., Kaufman, D. R., Albright, A., Cheng, J. D., Kang, S. P., Shankaran, V., Piha-Paul, S. A., Yearley, J., Seiwert, T. Y., Ribas, A., & McClanahan, T. K.

(2017). IFN-γ-related mRNA profile predicts clinical response to PD-1 blockade. The Journal of clinical investigation, 127(8), 2930–2940. https://doi.org/10.1172/JCI91190¶

Bagaev, A., Kotlov, N., Nomie, K., Svekolkin, V., Gafurov, A., Isaeva, O., Osokin, N., Kozlov, I., Frenkel, F., Gancharova, O., Almog, N., Tsiper, M., Ataullakhanov, R., & Fowler, N. (2021). Conserved pan-cancer microenvironment subtypes predict response to immunotherapy. Cancer cell, 39(6), 845–865.e7. https://doi.org/10.1016/j.ccell.2021.04.014

Bindea, G., Mlecnik, B., Tosolini, M., Kirilovsky, A., Waldner, M., Obenauf, A. C., Angell, H., Fredriksen, T., Lafontaine, L., Berger, A., Bruneval, P., Fridman, W. H., Becker, C., Pagès, F., Speicher, M. R., Trajanoski, Z., & Galon, J. (2013). Spatiotemporal dynamics of intratumoral immune cells reveal the immune landscape in human cancer. Immunity, 39(4), 782–795. https://doi.org/10.1016/j.immuni.2013.10.003

Borcherding, N., Vishwakarma, A., Voigt, A. P., Bellizzi, A., Kaplan, J., Nepple, K., Salem, A. K., Jenkins, R. W., Zakharia, Y., & Zhang, W. (2021). Mapping the immune environment in clear cell renal carcinoma by single-cell genomics. Communications biology, 4(1), 122. https://doi.org/10.1038/s42003-020-01625-6

Braun, D. A., Burke, K. P., & Van Allen, E. M. (2016). Genomic Approaches to Understanding Response and Resistance to Immunotherapy. Clinical cancer research : an official journal of the American Association for Cancer Research, 22(23), 5642–5650. https://doi.org/10.1158/1078-0432.CCR-16-0066

Braun, D. A., Hou, Y., Bakouny, Z., Ficial, M., Sant' Angelo, M., Forman, J., Ross-Macdonald, P., Berger, A. C., Jegede, O. A., Elagina, L., Steinharter, J., Sun, M., Wind-Rotolo, M., Pignon, J. C., Cherniack, A. D., Lichtenstein, L., Neuberg, D., Catalano, P., Freeman, G. J., Sharpe, A. H., … Choueiri, T. K. (2020). Interplay of somatic alterations and immune infiltration modulates response to PD-1 blockade in advanced clear cell renal cell carcinoma. Nature medicine, 26(6), 909–918. https://doi.org/10.1038/s41591-020-0839-y¶

Cabrita, R., Lauss, M., Sanna, A., Donia, M., Skaarup Larsen, M., Mitra, S., Johansson, I., Phung, B., Harbst, K., Vallon-Christersson, J., van Schoiack, A., Lövgren, K., Warren, S., Jirström, K., Olsson, H., Pietras, K., Ingvar, C., Isaksson, K., Schadendorf, D., Schmidt, H., … Jönsson, G. (2020). Tertiary lymphoid structures improve immunotherapy and survival in melanoma. Nature, 577(7791), 561–565. https://doi.org/10.1038/s41586-019-1914-8

Carter, S. L., Cibulskis, K., Helman, E., McKenna, A., Shen, H., Zack, T., Laird, P. W., Onofrio, R. C., Winckler, W., Weir, B. A., Beroukhim, R., Pellman, D., Levine, D. A., Lander, E. S., Meyerson, M., & Getz, G. (2012). Absolute quantification of somatic DNA alterations in human cancer. Nature biotechnology, 30(5), 413–421. https://doi.org/10.1038/nbt.2203

Danaher, P., Warren, S., Lu, R., Samayoa, J., Sullivan, A., Pekker, I., Wallden, B., Marincola, F. M., & Cesano, A. (2018). Pan-cancer adaptive immune resistance as defined by the Tumor Inflammation Signature (TIS): Results from The Cancer Genome Atlas (TCGA). Journal for ImmunoTherapy of Cancer, 6(1), 63. https://doi.org/10.1186/s40425-018-0367-1

de Vries-van Leeuwen, I. J., Kortekaas-Thijssen, C., Nzigou Mandouckou, J. A., Kas, S., Evidente, A., & de Boer, A. H. (2010). Fusicoccin-A selectively induces apoptosis in tumor cells after interferon-α priming. Cancer Letters, 293(2), 198–206. https://doi.org/10.1016/j.canlet.2010.01.009

Dieu-Nosjean, M. C., Goc, J., Giraldo, N. A., Sautès-Fridman, C., & Fridman, W. H. (2014). Tertiary lymphoid structures in cancer and beyond. Trends in immunology, 35(11), 571–580. https://doi.org/10.1016/j.it.2014.09.006

Draskau, M. K., Lardenois, A., Evrard, B., Boberg, J., Chalmel, F., & Svingen, T. (2021). Transcriptome analysis of fetal rat testis following intrauterine exposure to the azole fungicides triticonazole and flusilazole reveals subtle changes despite adverse endocrine effects. Chemosphere, 264(Pt 1), 128468. https://doi.org/10.1016/j.chemosphere.2020.128468

Drayton, D. L., Liao, S., Mounzer, R. H., & Ruddle, N. H. (2006). Lymphoid organ development: from ontogeny to neogenesis. Nature immunology, 7(4), 344–353. https://doi.org/10.1038/ni1330

Du, K., Wei, S., Wei, Z., Frederick, D. T., Miao, B., Moll, T., Tian, T., Sugarman, E., Gabrilovich, D. I., Sullivan, R. J., Liu, L., Flaherty, K. T., Boland, G. M., Herlyn, M., & Zhang, G. (2021). Pathway signatures derived from on-treatment tumor specimens predict response to anti-PD1 blockade in metastatic melanoma. Nature communications, 12(1), 6023. https://doi.org/10.1038/s41467-021-26299-4

Fridman, W. H., Zitvogel, L., Sautès-Fridman, C., & Kroemer, G. (2017). The immune contexture in cancer prognosis and treatment. Nature reviews. Clinical oncology, 14(12), 717–734. https://doi.org/10.1038/nrclinonc.2017.101

Germain, C., Gnjatic, S., & Dieu-Nosjean, M. C. (2015). Tertiary Lymphoid Structure-Associated B Cells are Key Players in Anti-Tumor Immunity. Frontiers in immunology, 6, 67. https://doi.org/10.3389/fimmu.2015.00067

Gupta, P., Wright, S. E., Kim, S.-H., & Srivastava, S. K. (2014). Phenethyl isothiocyanate: A comprehensive review of anti-cancer mechanisms. Biochimica et Biophysica Acta (BBA) - Reviews on Cancer, 1846(2), 405–424. https://doi.org/10.1016/j.bbcan.2014.08.003

Helmink, B. A., Reddy, S. M., Gao, J., Zhang, S., Basar, R., Thakur, R., Yizhak, K., Sade-Feldman, M., Blando, J., Han, G., Gopalakrishnan, V., Xi, Y., Zhao, H., Amaria, R. N., Tawbi, H. A., Cogdill, A. P., Liu, W., LeBleu, V. S., Kugeratski, F. G., Patel, S., ... Wargo, J. A. (2020). B cells and tertiary lymphoid structures promote immunotherapy response. Nature, 577(7791), 549–555. https://doi.org/10.1038/s41586-019-1922-8¶

Ho, T. H., Serie, D. J., Parasramka, M., Cheville, J. C., Bot, B. M., Tan, W., Wang, L., Joseph, R. W., Hilton, T., Leibovich, B. C., Parker, A. S., & Eckel-Passow, J. E. (2017). Differential gene expression profiling of matched primary renal cell carcinoma and metastases reveals upregulation of extracellular matrix genes. Annals of oncology : official journal of the European Society for Medical Oncology, 28(3), 604–610. https://doi.org/10.1093/annonc/mdw652

Hodi, F. S., O'Day, S. J., McDermott, D. F., Weber, R. W., Sosman, J. A., Haanen, J. B., Gonzalez, R., Robert, C., Schadendorf, D., Hassel, J. C., Akerley, W., van den Eertwegh, A. J., Lutzky, J., Lorigan, P., Vaubel, J. M., Linette, G. P., Hogg, D., Ottensmeier, C. H., Lebbé, C., Peschel, C., ... Urba, W. J. (2010). Improved survival with ipilimumab in patients with metastatic melanoma. The New England journal of medicine, 363(8), 711–723. https://doi.org/10.1056/NEJMoa1003466

Hu, J., Sun, F., Chen, W., Zhang, J., Zhang, T., Qi, M., Feng, T., Liu, H., Li, X., Xing, Y., Xiong, X., Shi, B., Zhou, G., & Han, B. (2019). BTF3 sustains cancer stem-like phenotype of prostate cancer via

stabilization of BMI1. Journal of experimental & clinical cancer research : CR, 38(1), 227. https://doi.org/10.1186/s13046-019-1222-z

Ke, S., Xie, F., Guo, Y., Chen, J., Wang, Z., Yu, Y., Geng, H., Xu, D., Liu, X., Xia, X., Yu, F., Zhu, C., Zhang, Z., Zhao, G., Li, B., & Zhao, W. (2022). High-level of intratumoral GITR+ CD4 T cells associate with poor prognosis in gastric cancer. iScience, 25(12), 105529. https://doi.org/10.1016/j.isci.2022.105529

Kusumawidjaja, G., Kayed, H., Giese, N., Bauer, A., Erkan, M., Giese, T., Hoheise, J. D., Friess, H., & Kleeff, J. (2007). Basic transcription factor 3 (BTF3) regulates transcription of tumor-associated genes in pancreatic cancer cells. Cancer biology & therapy, 6(3), 367–376. https://doi.org/10.4161/cbt.6.3.3704

Li, H., & Durbin, R. (2009). Fast and accurate short read alignment with Burrows-Wheeler transform. Bioinformatics (Oxford, England), 25(14), 1754–1760. https://doi.org/10.1093/bioinformatics/btp324

Li, X., Wang, C., Wang, S., Hu, Y., Jin, S., Liu, O., Gou, R., Nie, X., Liu, J., & Lin, B. (2021). YWHAE as an HE4 interacting protein can influence the malignant behaviour of ovarian cancer by regulating the PI3K/AKT and MAPK pathways. Cancer cell international, 21(1), 302. https://doi.org/10.1186/s12935-021-01989-7

Lin, J., Yu, M., Xu, X., Wang, Y., Xing, H., An, J., Yang, J., Tang, C., Sun, D., & Zhu, Y. (2020). Identification of biomarkers related to CD8+ T cell infiltration with gene co-expression network in clear cell renal cell carcinoma. Aging, 12(4), 3694–3712. https://doi.org/10.18632/aging.102841

Liu, D., Schilling, B., Liu, D., Sucker, A., Livingstone, E., Jerby-Arnon, L., Zimmer, L., Gutzmer, R., Satzger, I., Loquai, C., Grabbe, S., Vokes, N., Margolis, C. A., Conway, J., He, M. X., Elmarakeby, H., Dietlein, F., Miao, D., Tracy, A., Gogas, H., … Schadendorf, D. (2019). Integrative molecular and clinical modeling of clinical outcomes to PD1 blockade in patients with metastatic melanoma. Nature medicine, 25(12), 1916–1927. https://doi.org/10.1038/s41591-019-0654-5

Lohr, M., Edlund, K., Botling, J., Hammad, S., Hellwig, B., Othman, A., Berglund, A., Lambe, M., Holmberg, L., Ekman, S., Bergqvist, M., Pontén, F., Cadenas, C., Marchan, R., Hengstler, J. G., Rahnenführer, J., & Micke, P. (2013). The prognostic relevance of tumour-infiltrating plasma cells and immunoglobulin kappa C indicates an important role of the humoral immune response in non-small cell lung cancer. Cancer letters, 333(2), 222–228. https://doi.org/10.1016/j.canlet.2013.01.036

McDermott, D. F., Huseni, M. A., Atkins, M. B., Motzer, R. J., Rini, B. I., Escudier, B., Fong, L., Joseph, R. W., Pal, S. K., Reeves, J. A., Sznol, M., Hainsworth, J., Rathmell, W. K., Stadler, W. M., Hutson, T., Gore, M. E., Ravaud, A., Bracarda, S., Suárez, C., … Powles, T. (2018). Clinical activity and molecular correlates of response to atezolizumab alone or in combination with bevacizumab versus sunitinib in renal cell carcinoma. Nature Medicine, 24(6), 749–757. https://doi.org/10.1038/s41591-018-0053-3

McGrail, D. J., Pilié, P. G., Rashid, N. U., Voorwerk, L., Slagter, M., Kok, M., Jonasch, E., Khasraw, M., Heimberger, A. B., Lim, B., Ueno, N. T., Litton, J. K., Ferrarotto, R., Chang, J. T., Moulder, S. L., & Lin, S. Y. (2021). High tumor mutation burden fails to predict immune checkpoint blockade response across all cancer types. Annals of oncology : official journal of the European Society for Medical Oncology, 32(5), 661–672. https://doi.org/10.1016/j.annonc.2021.02.006

Motzer, R. J., Tannir, N. M., McDermott, D. F., Arén Frontera, O., Melichar, B., Choueiri, T. K., Plimack, E. R., Barthélémy, P., Porta, C., George, S., Powles, T., Donskov, F., Neiman, V., Kollmannsberger, C. K.,

Salman, P., Gurney, H., Hawkins, R., Ravaud, A., Grimm, M. O., Bracarda, S., … CheckMate 214 Investigators (2018). Nivolumab plus Ipilimumab versus Sunitinib in Advanced Renal-Cell Carcinoma. The New England journal of medicine, 378(14), 1277–1290. https://doi.org/10.1056/NEJMoa1712126

Newman, A. M., Steen, C. B., Liu, C. L., Gentles, A. J., Chaudhuri, A. A., Scherer, F., Khodadoust, M. S., Esfahani, M. S., Luca, B. A., Steiner, D., Diehn, M., & Alizadeh, A. A. (2019). Determining cell type abundance and expression from bulk tissues with digital cytometry. Nature biotechnology, 37(7), 773–782. https://doi.org/10.1038/s41587-019-0114-2¶

Obradovic, A., Chowdhury, N., Haake, S. M., Ager, C., Wang, V., Vlahos, L., Guo, X. V., Aggen, D. H., Rathmell, W. K., Jonasch, E., Johnson, J. E., Roth, M., Beckermann, K. E., Rini, B. I., McKiernan, J., Califano, A., & Drake, C. G. (2021). Single-cell protein activity analysis identifies recurrence-associated renal tumor macrophages. Cell, 184(11), 2988–3005.e16. https://doi.org/10.1016/j.cell.2021.04.038

Oldham, K. A., Parsonage, G., Bhatt, R. I., Wallace, D. M., Deshmukh, N., Chaudhri, S., Adams, D. H., & Lee, S. P. (2012). T lymphocyte recruitment into renal cell carcinoma tissue: a role for chemokine receptors CXCR3, CXCR6, CCR5, and CCR6. European urology, 61(2), 385–394. https://doi.org/10.1016/j.eururo.2011.10.035

Petitprez, F., Meylan, M., de Reyniès, A., Sautès-Fridman, C., & Fridman, W. H. (2020). The Tumor Microenvironment in the Response to Immune Checkpoint Blockade Therapies. Frontiers in immunology, 11, 784. https://doi.org/10.3389/fimmu.2020.00784

Riaz, N., Havel, J. J., Makarov, V., Desrichard, A., Urba, W. J., Sims, J. S., Hodi, F. S., Martín-Algarra, S., Mandal, R., Sharfman, W. H., Bhatia, S., Hwu, W. J., Gajewski, T. F., Slingluff, C. L., Jr, Chowell, D., Kendall, S. M., Chang, H., Shah, R., Kuo, F., Morris, L. G. T., … Chan, T. A. (2017). Tumor and Microenvironment Evolution during Immunotherapy with Nivolumab. Cell, 171(4), 934–949.e16. https://doi.org/10.1016/j.cell.2017.09.028

Schadendorf, D., Hodi, F. S., Robert, C., Weber, J. S., Margolin, K., Hamid, O., Patt, D., Chen, T. T., Berman, D. M., & Wolchok, J. D. (2015). Pooled Analysis of Long-Term Survival Data From Phase II and Phase III Trials of Ipilimumab in Unresectable or Metastatic Melanoma. Journal of clinical oncology : official journal of the American Society of Clinical Oncology, 33(17), 1889–1894. https://doi.org/10.1200/JCO.2014.56.2736

Schmidt, M., Böhm, D., von Törne, C., Steiner, E., Puhl, A., Pilch, H., Lehr, H. A., Hengstler, J. G., Kölbl, H., & Gehrmann, M. (2008). The humoral immune system has a key prognostic impact in node-negative breast cancer. Cancer research, 68(13), 5405–5413. https://doi.org/10.1158/0008-5472.CAN-07-5206

Şenbabaoğlu, Y., Gejman, R. S., Winer, A. G., Liu, M., Van Allen, E. M., de Velasco, G., Miao, D., Ostrovnaya, I., Drill, E., Luna, A., Weinhold, N., Lee, W., Manley, B. J., Khalil, D. N., Kaffenberger, S. D., Chen, Y., Danilova, L., Voss, M. H., Coleman, J. A., Russo, P., … Hakimi, A. A. (2016). Tumor immune microenvironment characterization in clear cell renal cell carcinoma identifies prognostic and immunotherapeutically relevant messenger RNA signatures. Genome biology, 17(1), 231. https://doi.org/10.1186/s13059-016-1092-z

Symes, A. J., Eilertsen, M., Millar, M., Nariculam, J., Freeman, A., Notara, M., Feneley, M. R., Patel, H. R., Masters, J. R., & Ahmed, A. (2013). Quantitative analysis of BTF3, HINT1, NDRG1 and ODC1 protein

over-expression in human prostate cancer tissue. PloS one, 8(12), e84295. https://doi.org/10.1371/journal.pone.0084295

Trefny, M. P., Rothschild, S. I., Uhlenbrock, F., Rieder, D., Kasenda, B., Stanczak, M. A., Berner, F., Kashyap, A. S., Kaiser, M., Herzig, P., Poechtrager, S., Thommen, D. S., Geier, F., Savic, S., Jermann, P., Alborelli, I., Schaub, S., Stenner, F., Früh, M., Trajanoski, Z., … Läubli, H. (2019). A Variant of a Killer Cell Immunoglobulin-like Receptor Is Associated with Resistance to PD-1 Blockade in Lung Cancer. Clinical cancer research : an official journal of the American Association for Cancer Research, 25(10), 3026–3034. https://doi.org/10.1158/1078-0432.CCR-18-3041

van Herpen, C. M., van der Voort, R., van der Laak, J. A., Klasen, I. S., de Graaf, A. O., van Kempen, L. C., de Vries, I. J., Boer, T. D., Dolstra, H., Torensma, R., van Krieken, J. H., Adema, G. J., & De Mulder, P. H. (2008). Intratumoral rhIL-12 administration in head and neck squamous cell carcinoma patients induces B cell activation. International journal of cancer, 123(10), 2354–2361. https://doi.org/10.1002/ijc.23756

Wang, H., Xing, J., Wang, W., Lv, G., He, H., Lu, Y., Sun, M., Chen, H., & Li, X. (2021). Molecular Characterization of the Oncogene BTF3 and Its Targets in Colorectal Cancer. Frontiers in cell and developmental biology, 8, 601502. https://doi.org/10.3389/fcell.2020.601502

Wang, X., Park, J., Susztak, K., Zhang, N. R., & Li, M. (2019). Bulk tissue cell type deconvolution with multi-subject single-cell expression reference. Nature communications, 10(1), 380. https://doi.org/10.1038/s41467-018-08023-x

Wood, M. A., Weeder, B. R., David, J. K., Nellore, A., & Thompson, R. F. (2020). Burden of tumor mutations, neoepitopes, and other variants are weak predictors of cancer immunotherapy response and overall survival. Genome medicine, 12(1), 33. https://doi.org/10.1186/s13073-020-00729-2

Wu, C. C., Wang, Y. A., Livingston, J. A., Zhang, J., & Futreal, P. A. (2022). Prediction of biomarkers and therapeutic combinations for anti-PD-1 immunotherapy using the global gene network association. Nature communications, 13(1), 42. https://doi.org/10.1038/s41467-021-27651-4

Yoshihara, K., Shahmoradgoli, M., Martínez, E., Vegesna, R., Kim, H., Torres-Garcia, W., Treviño, V., Shen, H., Laird, P. W., Levine, D. A., Carter, S. L., Getz, G., Stemke-Hale, K., Mills, G. B., & Verhaak, R. G. (2013). Inferring tumour purity and stromal and immune cell admixture from expression data. Nature communications, 4, 2612. https://doi.org/10.1038/ncomms3612

Yuan, J.-M., Stepanov, I., Murphy, S. E., Wang, R., Allen, S., Jensen, J., Strayer, L., Adams-Haduch, J., Upadhyaya, P., Le, C., Kurzer, M. S., Nelson, H. H., Yu, M. C., Hatsukami, D., & Hecht, S. S. (2016). Clinical Trial of 2-Phenethyl Isothiocyanate as an Inhibitor of Metabolic Activation of a Tobacco-Specific Lung Carcinogen in Cigarette Smokers. Cancer Prevention Research, 9(5), 396–405. https://doi.org/10.1158/1940-6207.CAPR-15-0380

Zhang, C., Li, Z., Qi, F., Hu, X., & Luo, J. (2019). Exploration of the relationships between tumor mutation burden with immune infiltrates in clear cell renal cell carcinoma. Annals of translational medicine, 7(22), 648. https://doi.org/10.21037/atm.2019.10.84

Zhang, L., Conejo-Garcia, J. R., Katsaros, D., Gimotty, P. A., Massobrio, M., Regnani, G., Makrigiannakis, A., Gray, H., Schlienger, K., Liebman, M. N., Rubin, S. C., & Coukos, G. (2003). Intratumoral T cells,

recurrence, and survival in epithelial ovarian cancer. The New England journal of medicine, 348(3), 203–213. https://doi.org/10.1056/NEJMoa020177

Zhang, S., He, Y., Xuan, Q., Ling, X., Men, K., Zhao, X., Xue, D., Li, L., & Zhang, Y. (2022). TMEM139 prevents NSCLC metastasis by inhibiting lysosomal degradation of E-cadherin. Cancer science, 113(6), 1999–2007. https://doi.org/10.1111/cas.15341

Acknowledgements

The study was supported by the KATY project, which has received funding from the European Union's Horizon 2020 research and innovation program under grant agreement No 101017453 and by the CANVAS project, which has received funding from the Horizon Europe twinning program under grant agreement No 101079510. Most of the computations presented in this paper were performed using the GRICAD infrastructure (https://gricad.univ-grenoble-alpes.fr), which is supported by Grenoble research communities.

Figure legends

Fig. 1 Extended annotation of ccRCC microenvironment cell types from single-cell RNA-Seq from Obradovic et al. A. UMAP of the CD45-positive cells. B. UMAP of the CD45-negative cells. C. Distribution of the cell type proportions.

Fig. 2 Computational assessment of cell fractions estimated by cell deconvolution. A. Correlation levels between simulated pseudo bulk single-cell RNA-seq mixtures with known proportions and fractions predicted by cell deconvolution using CIBERSORTx. Correlation values are assessed using Spearman correlation coefficients, slopes of the best linear regression line and inverse of the RMSE values. B. Correlation between tumor purity values calculated by ESTIMATE method and tumor fractions estimated by CIBERSORTx. C. Correlation between tumor purity values calculated by ABSOLUTE method and tumor fractions estimated by CIBERSORTx.

Fig. 3 Experimental evaluation of cell fractions estimated by cell deconvolution. A. Examples of single plex immunofluorescence for CD8+, CD34+, and CD45+ cells (left panel: red for CD8, center panel: yellow for CD34, right panel: green for CD45). Hoechst counterstaining. B. Distribution of estimated cell fractions of CD8+, CD34+ and CD45+ cells for ccRCC tissue samples. C. Correlation between IHC-based and CIBERSORTx-based quantification of CD8+, CD34+ and CD45+ cells from 19, 13 and 19 matched tumors, respectively.

Fig. 4 TME subtypes of ccRCC metastases related to ICB treatment response A. Selection of pre-treatment metastatic site samples from CheckMate cohort patients treated with nivolumab. B. Measures of cell fractions estimated by CIBERSORTx according to ICB clinical benefit. C. Consensus clustering of the metastatic site samples into 3 TME subtypes using cell types associated with ICB treatment response (black rectangles represent missing values). D. Measures of cell fractions of CD8 T cells and plasma cells according to TME subtypes. E. OS and PFS values based on TME subtypes. F. Published gene signature values according to TME subtypes.

Fig. 5 Immunoglobulin gene expressions associated with TME subtypes A. Selection of genes according to single-cell RNA-Seq DEG analysis and TME-subtypes. B. Measures of gene expressions related to TME subtypes. C. Consensus clustering of the metastatic site samples into 4 clusters based on genes related to TME-subtypes (black rectangles represent missing values). D. PFS and E. OS values based on G1-G4 clusters. .

Fig. 6 Tumor-Immunity Differential (TID) score associated with ICB treatment response. A. ROC curves and AUC-ROC values for estimated cell fractions and gene expressions related to ICB treatment response. B. TID score formula (*The tumor part is the sum of the tumor fraction and the TMB values, **The immunity part is the sum of the T-CD8, Plasma B and T regulatory fractions and the PDCD1 gene values). C. Consensus clustering of metastatic site samples based on the TID score (black rectangles represent missing values). D. Published gene signature values according to TID subtypes E. PFS and F. OS values based on TID subtypes. G. Expression of differentially expressed

genes between TID subtypes. H. Consensus clustering of the metastatic site samples into 2 clusters, TID-G1 and TID-G2 subtypes, based on genes related to TID subtypes (black rectangles represent missing values). I. PFS and J. OS values following TID-G1 and TID-G2 clusters.

Fig. 7 TID score and TID-related genes as key markers of ICB treatment response in several cancer types. A. Classification performances of responders (R) over non-responders (NR) samples for a collection of predictive scores and genes calculated from cohorts of pre-treated (before Nivolumab treatment) ccRCC samples. B. Correlation between scores calculated for 15 patients with matched ccRCC primary and metastatic site samples. Classification performances of R over NR for C. pre-treated melanoma and NSCLC (PBMCs) samples and D. on-treatment melanoma and NSCLC (PBMCs) samples.

Figure 1

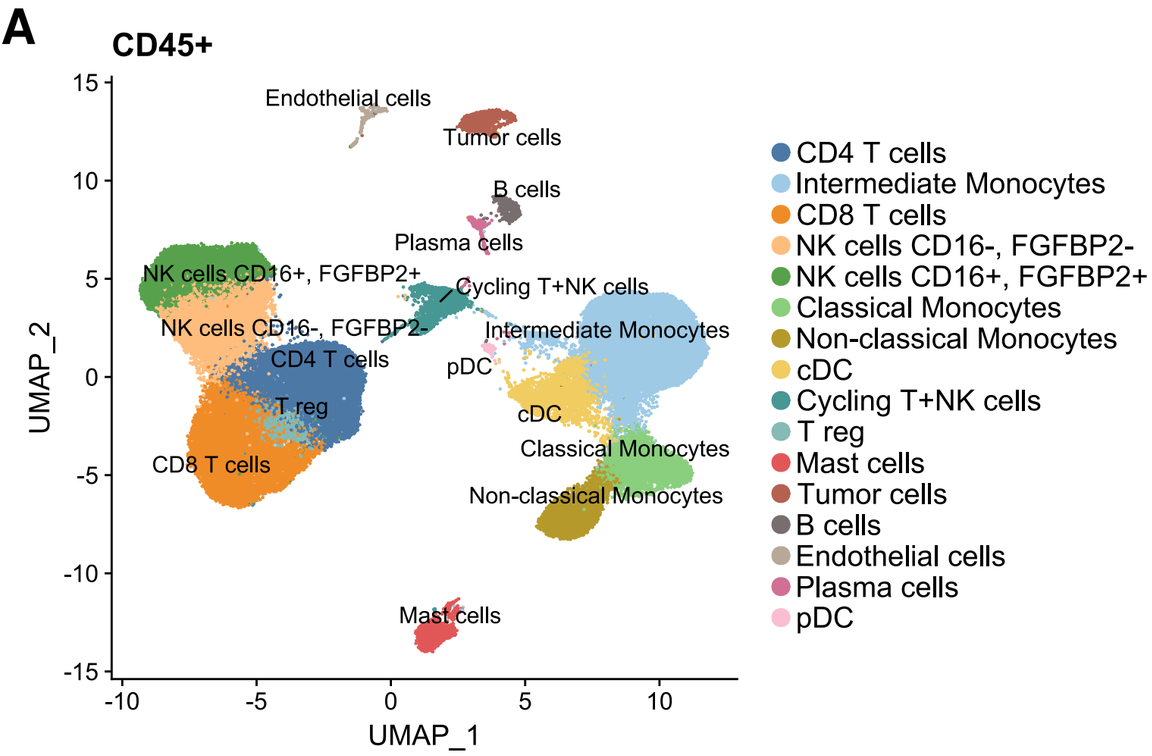
A
CD45+
Endothelial cells
Tumor cells
B cells
Plasma cells
NK cells CD16+, FGFBP2+
Cycling T+NK cells
NK cells CD16-, FGFBP2-
Intermediate Monocytes
CD4 T cells
pDC
T reg
cDC
Classical Monocytes
CD8 T cells
Non-classical Monocytes
Mast cells
UMAP_2
UMAP_1
CD4 T cells
Intermediate Monocytes
CD8 T cells
NK cells CD16-, FGFBP2-
NK cells CD16+, FGFBP2+
Classical Monocytes
Non-classical Monocytes
cDC
Cycling T+NK cells
T reg
Mast cells
Tumor cells
B cells
Endothelial cells
Plasma cells
pDC

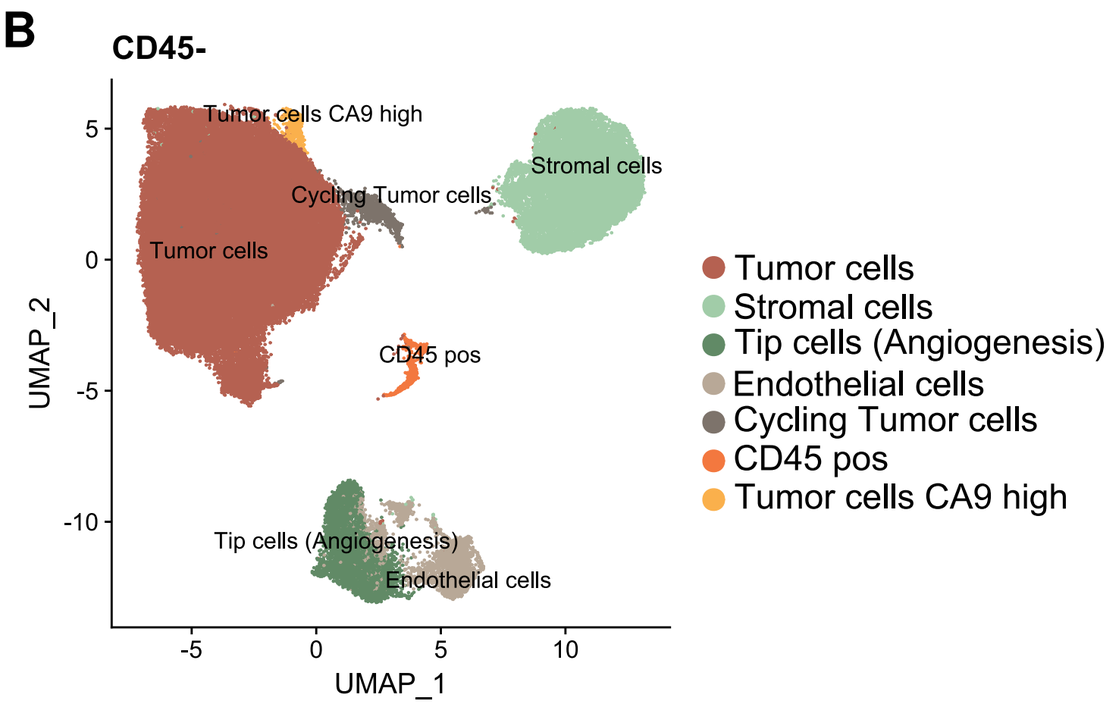
B
CD45-
Tumor cells CA9 high
Stromal cells
Cycling Tumor cells
Tumor cells
CD45 pos
Tip cells (Angiogenesis)
Endothelial cells
UMAP_2
UMAP_1
Tumor cells
Stromal cells
Tip cells (Angiogenesis)
Endothelial cells
Cycling Tumor cells
CD45 pos
Tumor cells CA9 high

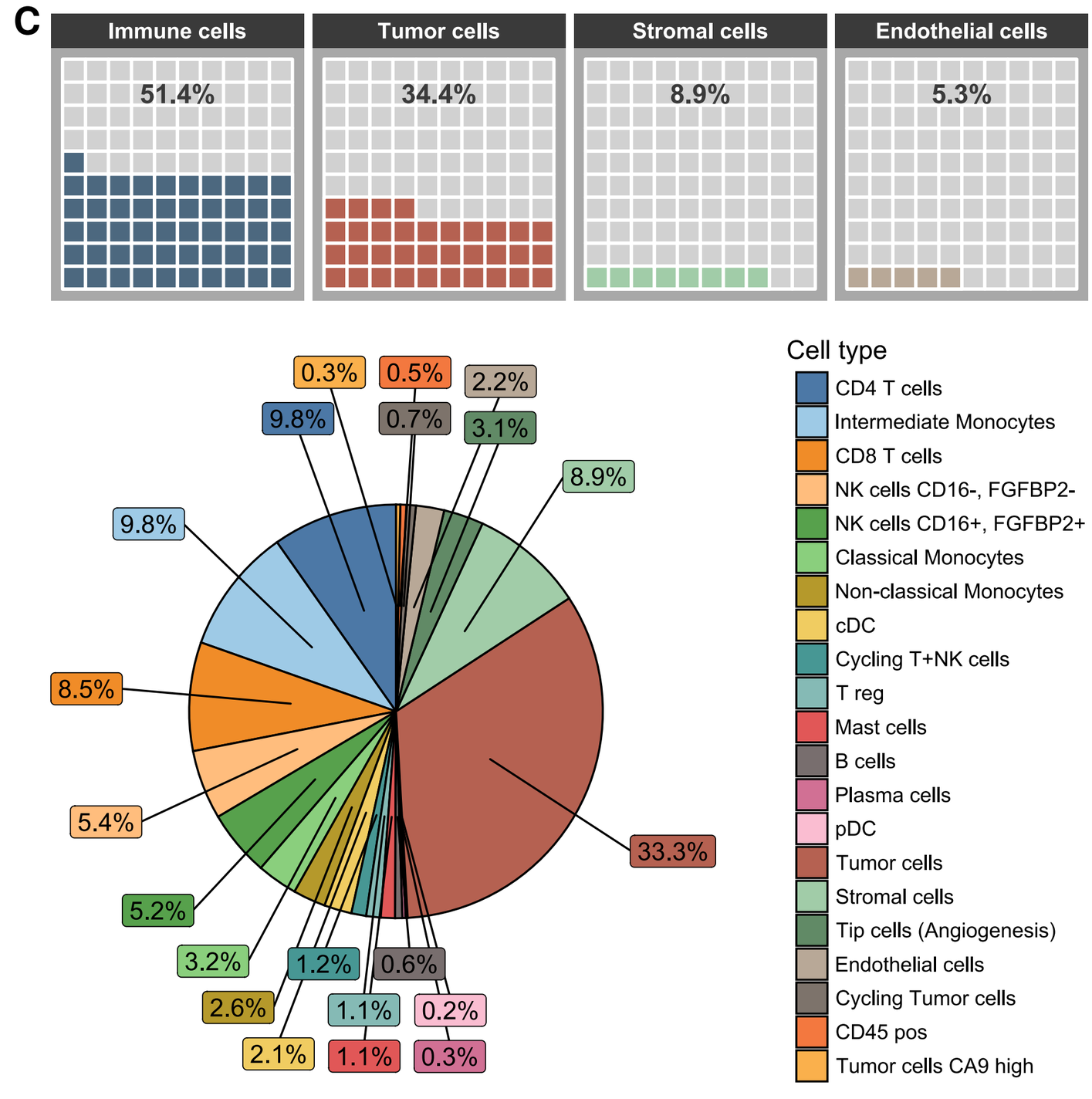
C
Immune cells
51.4%
Tumor cells
34.4%
Stromal cells
8.9%
Endothelial cells
5.3%
0.3%
0.5%
2.2%
9.8%
0.7%
3.1%
8.9%
9.8%
8.5%
5.4%
33.3%
5.2%
3.2%
1.2%
0.6%
2.6%
1.1%
0.2%
2.1%
1.1%
0.3%
Cell type
CD4 T cells
Intermediate Monocytes
CD8 T cells
NK cells CD16-, FGFBP2-
NK cells CD16+, FGFBP2+
Classical Monocytes
Non-classical Monocytes
cDC
Cycling T+NK cells
T reg
Mast cells
B cells
Plasma cells
pDC
Tumor cells
Stromal cells
Tip cells (Angiogenesis)
Endothelial cells
Cycling Tumor cells
CD45 pos
Tumor cells CA9 high

Figure 2

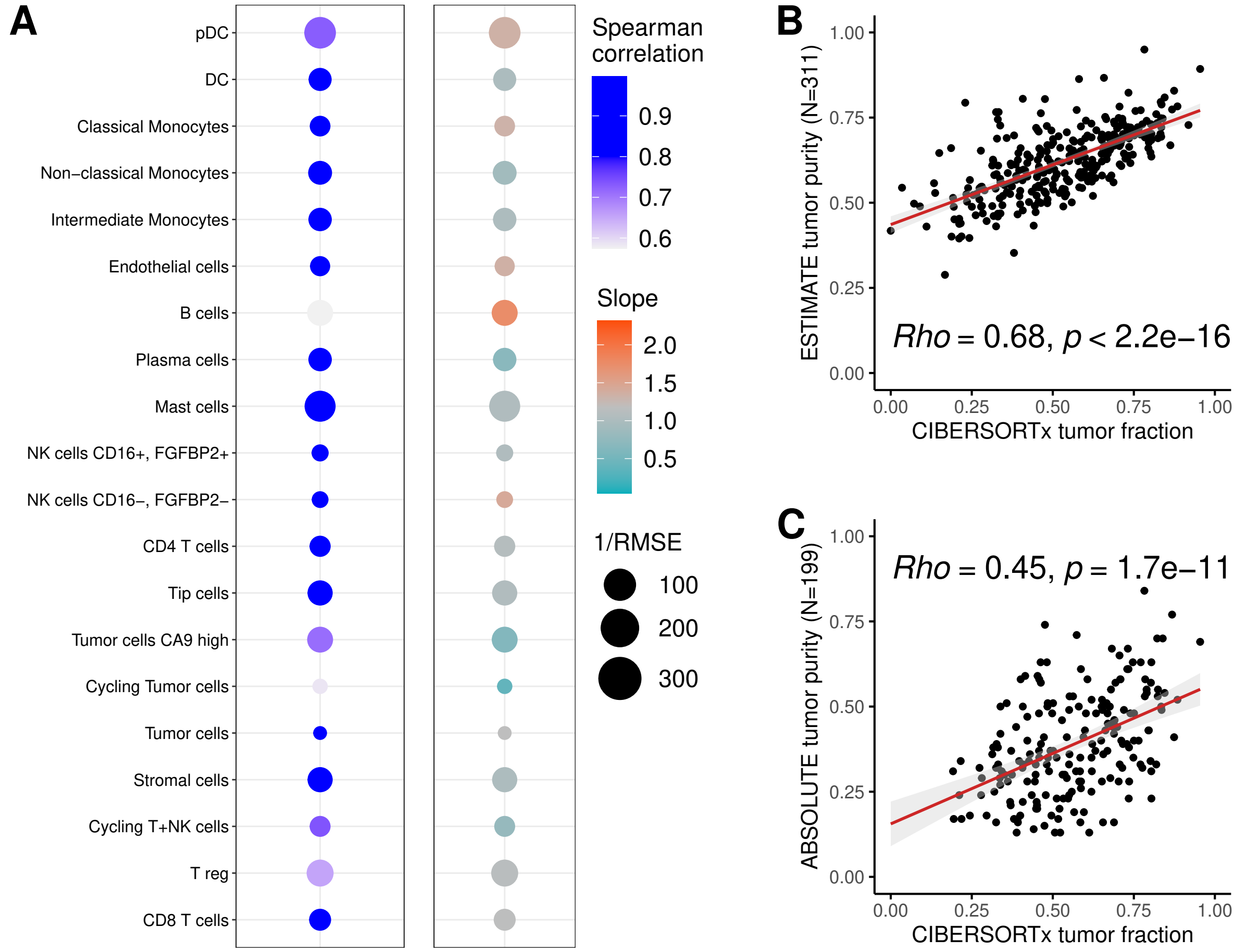
A
pDC
DC
Classical Monocytes
Non−classical Monocytes
Intermediate Monocytes
Endothelial cells
B cells
Plasma cells
Mast cells
NK cells CD16+, FGFBP2+
NK cells CD16−, FGFBP2−
CD4 T cells
Tip cells
Tumor cells CA9 high
Cycling Tumor cells
Tumor cells
Stromal cells
Cycling T+NK cells
T reg
CD8 T cells
Spearman correlation
0.9
0.8
0.7
0.6
Slope
2.0
1.5
1.0
0.5
1/RMSE
100
200
300
B
ESTIMATE tumor purity (N=311)
CIBERSORTx tumor fraction
Rho = 0.68, p < 2.2e−16
C
ABSOLUTE tumor purity (N=199)
CIBERSORTx tumor fraction
Rho = 0.45, p = 1.7e−11

Figure 3

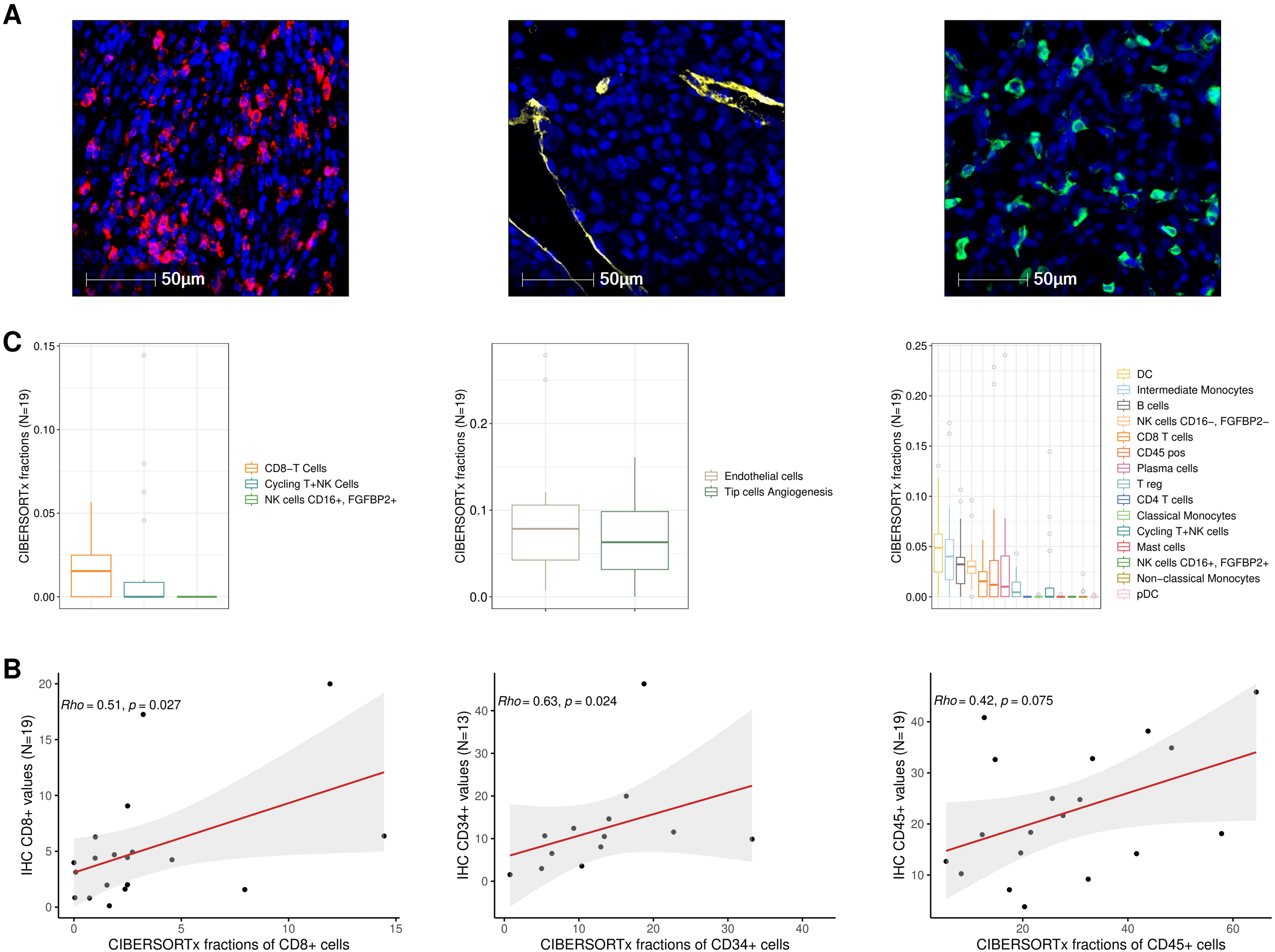
A
50µm
50µm
50µm
C
CIBERSORTx fractions (N=19)
CD8−T Cells
Cycling T+NK Cells
NK cells CD16+, FGFBP2+
Endothelial cells
Tip cells Angiogenesis
DC
Intermediate Monocytes
B cells
NK cells CD16−, FGFBP2−
CD8 T cells
CD45 pos
Plasma cells
T reg
CD4 T cells
Classical Monocytes
Cycling T+NK cells
Mast cells
NK cells CD16+, FGFBP2+
Non−classical Monocytes
pDC
B
Rho = 0.51, p = 0.027
IHC CD8+ values (N=19)
CIBERSORTx fractions of CD8+ cells
Rho = 0.63, p = 0.024
IHC CD34+ values (N=13)
CIBERSORTx fractions of CD34+ cells
Rho = 0.42, p = 0.075
IHC CD45+ values (N=19)
CIBERSORTx fractions of CD45+ cells

Figure 4

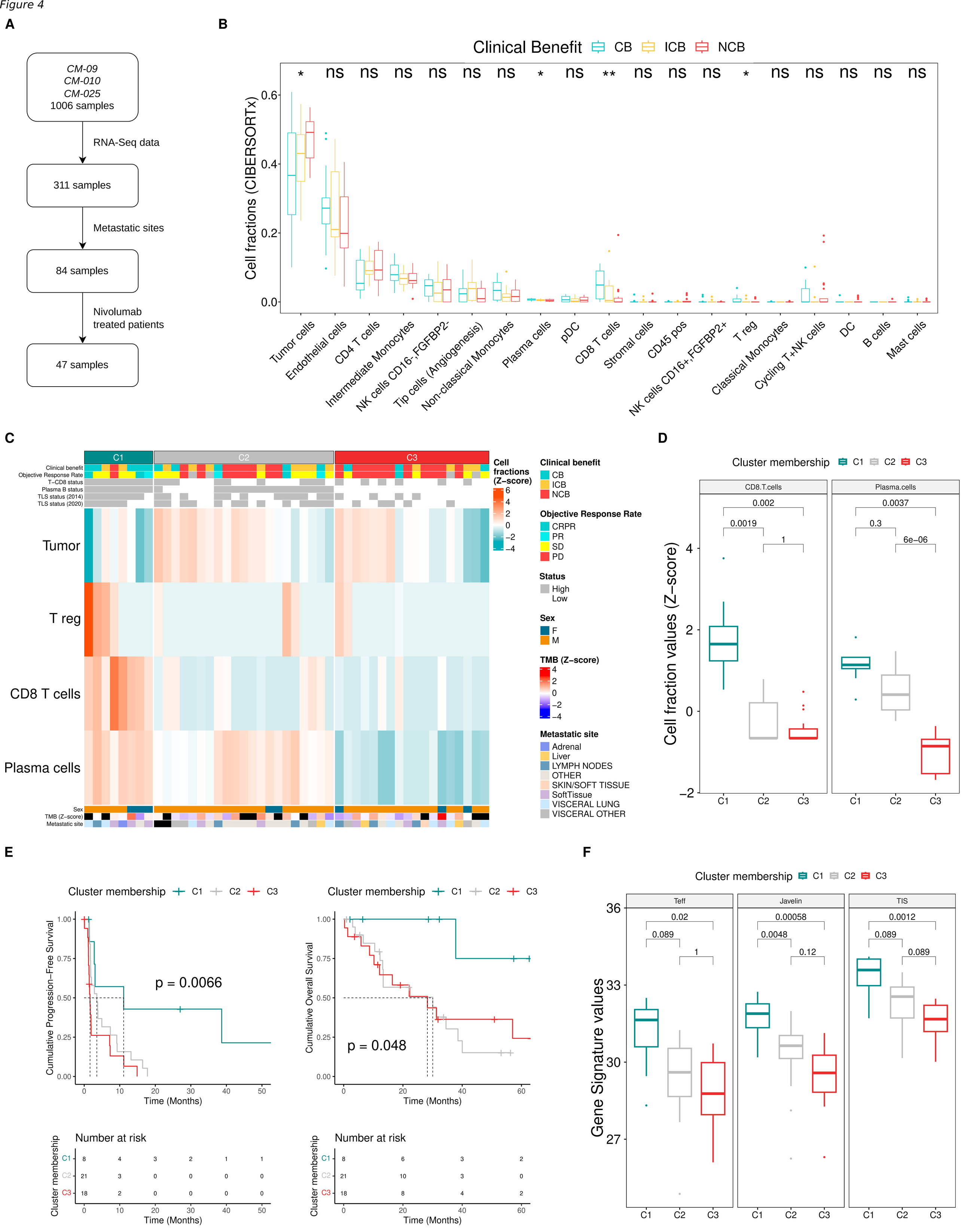
A
CM-09
CM-010
CM-025
1006 samples
RNA-Seq data
311 samples
Metastatic sites
84 samples
Nivolumab treated patients
47 samples
B
Clinical Benefit CB ICB NCB
Cell fractions (CIBERSORTx)
Tumor cells
Endothelial cells
CD4 T cells
Intermediate Monocytes
NK cells CD16-,FGFBP2-
Tip cells (Angiogenesis)
Non-classical Monocytes
Plasma cells
pDC
CD8 T cells
Stromal cells
CD45 pos
NK cells CD16+,FGFBP2+
T reg
Classical Monocytes
Cycling T+NK cells
DC
B cells
Mast cells
C
C1
C2
C3
Clinical benefit
Objective Response Rate
T-CD8 status
Plasma B status
TLS status (2014)
TLS status (2020)
Tumor
T reg
CD8 T cells
Plasma cells
Sex
TMB (Z-score)
Metastatic site
Cell fractions (Z-score)
Clinical benefit
CB
ICB
NCB
Objective Response Rate
CRPR
PR
SD
PD
Status
High
Low
Sex
F
M
TMB (Z-score)
Metastatic site
Adrenal
Liver
LYMPH NODES
OTHER
SKIN/SOFT TISSUE
SoftTissue
VISCERAL LUNG
VISCERAL OTHER
D
Cluster membership C1 C2 C3
CD8.T.cells
Plasma.cells
Cell fraction values (Z-score)
E
Cluster membership C1 C2 C3
Cumulative Progression-Free Survival
p = 0.0066
Time (Months)
Number at risk
Cumulative Overall Survival
p = 0.048
F
Cluster membership C1 C2 C3
Teff
Javelin
TIS
Gene Signature values

Figure 5

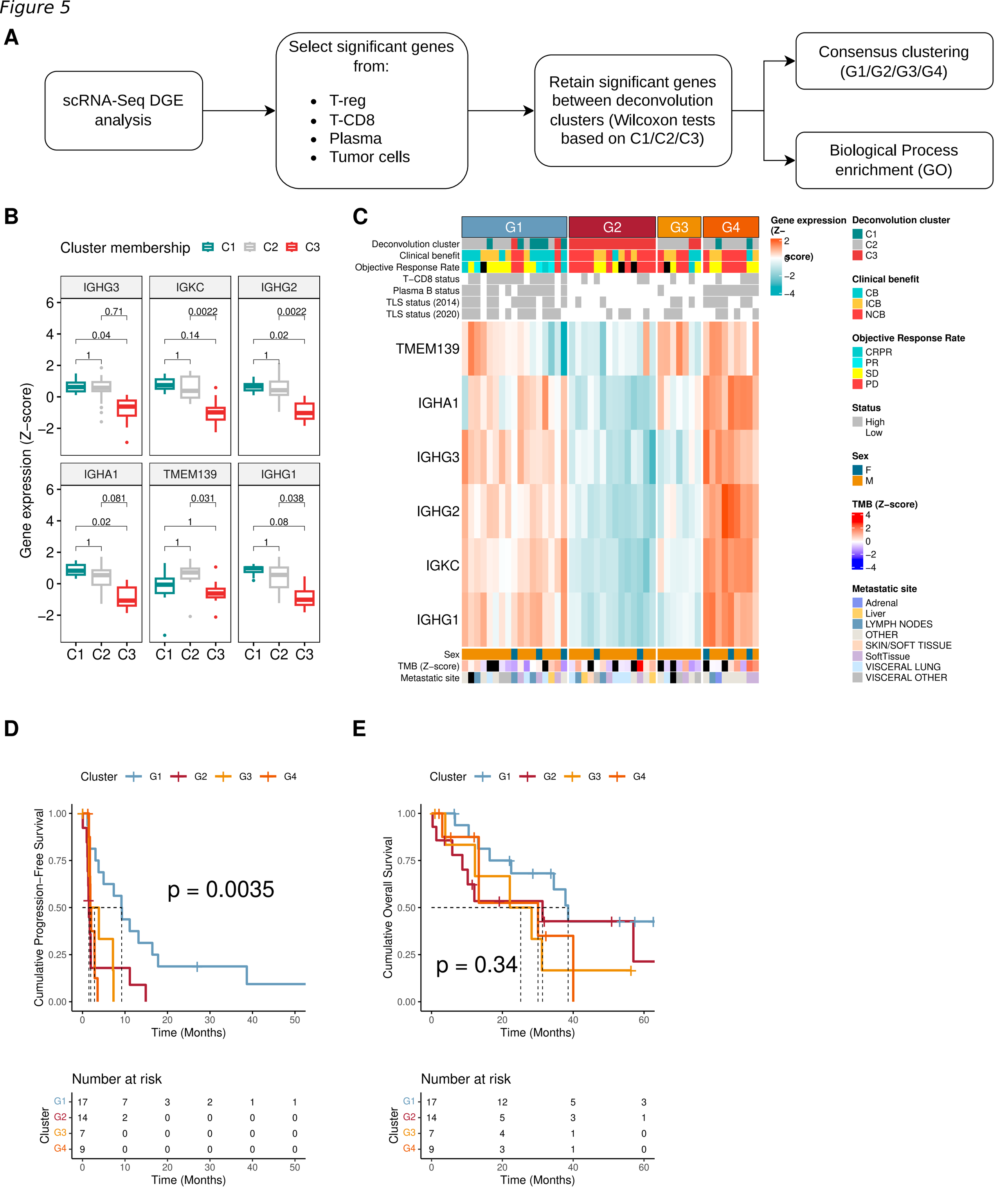
A
scRNA-Seq DGE analysis
Select significant genes from:
T-reg
T-CD8
Plasma
Tumor cells
Retain significant genes between deconvolution clusters (Wilcoxon tests based on C1/C2/C3)
Consensus clustering (G1/G2/G3/G4)
Biological Process enrichment (GO)
B
Cluster membership C1 C2 C3
IGHG3
IGKC
IGHG2
IGHA1
TMEM139
IGHG1
Gene expression (Z-score)
C1 C2 C3
C
G1 G2 G3 G4
Deconvolution cluster
Clinical benefit
Objective Response Rate
T-CD8 status
Plasma B status
TLS status (2014)
TLS status (2020)
TMEM139
IGHA1
IGHG3
IGHG2
IGKC
IGHG1
Sex
TMB (Z-score)
Metastatic site
Gene expression (Z-score)
Deconvolution cluster C1 C2 C3
Clinical benefit CB ICB NCB
Objective Response Rate CRPR PR SD PD
Status High Low
Sex F M
TMB (Z-score)
Metastatic site Adrenal Liver LYMPH NODES OTHER SKIN/SOFT TISSUE SoftTissue VISCERAL LUNG VISCERAL OTHER
D
Cluster G1 G2 G3 G4
Cumulative Progression-Free Survival
p = 0.0035
Time (Months)
Number at risk
Cluster
G1 17 7 3 2 1 1
G2 14 2 0 0 0 0
G3 7 0 0 0 0 0
G4 9 0 0 0 0 0
E
Cluster G1 G2 G3 G4
Cumulative Overall Survival
p = 0.34
Time (Months)
Number at risk
Cluster
G1 17 12 5 3
G2 14 5 3 1
G3 7 4 1 0
G4 9 3 1 0

Figure 6

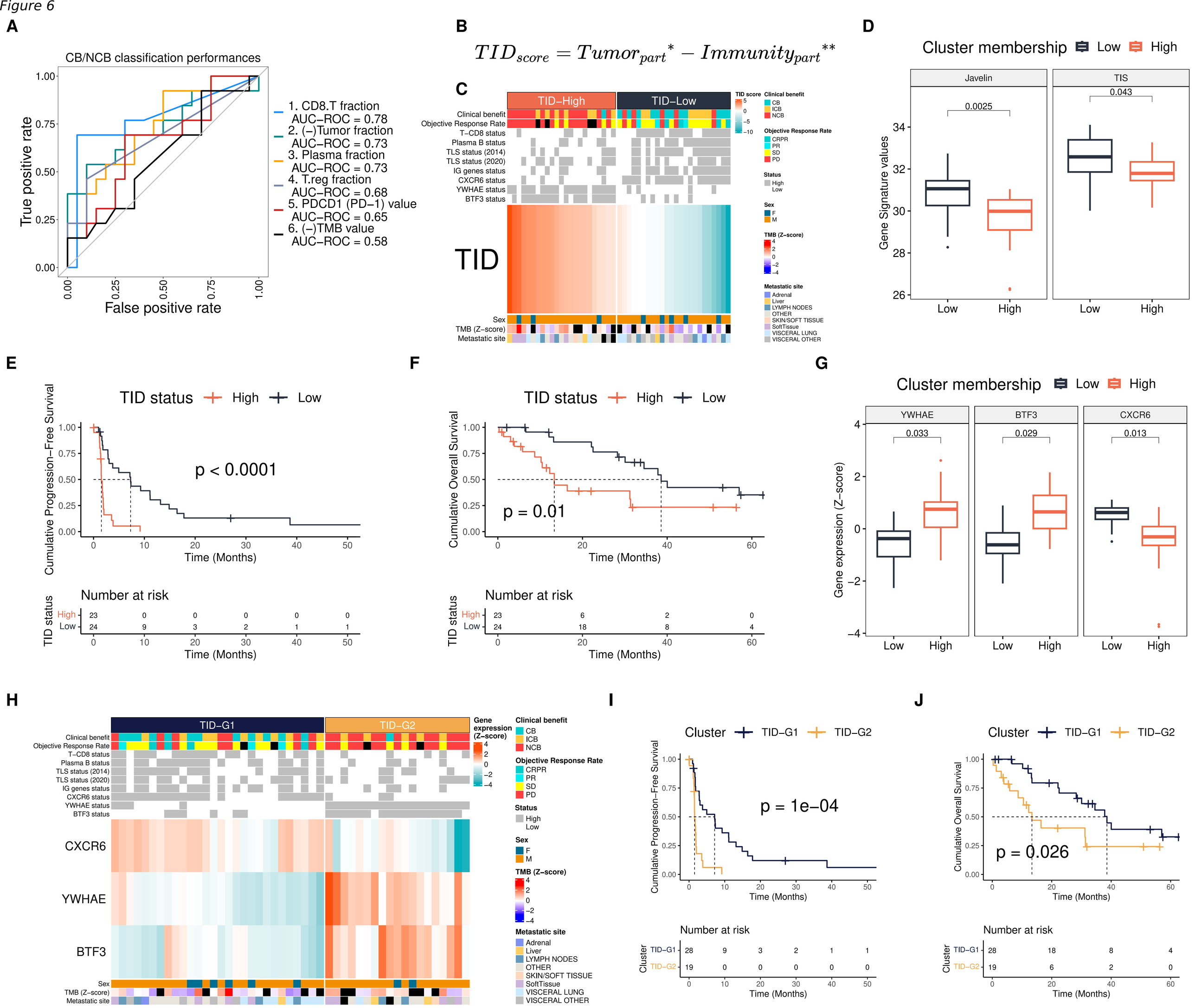
A
CB/NCB classification performances
True positive rate
False positive rate
1. CD8.T fraction AUC−ROC = 0.78
2. (−)Tumor fraction AUC−ROC = 0.73
3. Plasma fraction AUC−ROC = 0.73
4. T.reg fraction AUC−ROC = 0.68
5. PDCD1 (PD−1) value AUC−ROC = 0.65
6. (−)TMB value AUC−ROC = 0.58
B
$TID_{score} = Tumor_{part}{}^{*} - Immunity_{part}{}^{**}$
C
TID−High
TID−Low
Clinical benefit
Objective Response Rate
T−CD8 status
Plasma B status
TLS status (2014)
TLS status (2020)
IG genes status
CXCR6 status
YWHAE status
BTF3 status
TID
Sex
TMB (Z−score)
Metastatic site
TID score
Clinical benefit
CB
ICB
NCB
Objective Response Rate
CRPR
PR
SD
PD
Status
High
Low
Sex
F
M
TMB (Z−score)
Metastatic site
Adrenal
Liver
LYMPH NODES
OTHER
SKIN/SOFT TISSUE
SoftTissue
VISCERAL LUNG
VISCERAL OTHER
D
Cluster membership Low High
Javelin
TIS
0.0025
0.043
Gene Signature values
Low
High
E
TID status High Low
Cumulative Progression−Free Survival
p < 0.0001
Time (Months)
Number at risk
TID status
High 23 0 0 0 0 0
Low 24 9 3 2 1 1
F
TID status High Low
Cumulative Overall Survival
p = 0.01
Time (Months)
Number at risk
TID status
High 23 6 2 0
Low 24 18 8 4
G
Cluster membership Low High
YWHAE
BTF3
CXCR6
0.033
0.029
0.013
Gene expression (Z−score)
Low
High
H
TID−G1
TID−G2
Clinical benefit
Objective Response Rate
T−CD8 status
Plasma B status
TLS status (2014)
TLS status (2020)
IG genes status
CXCR6 status
YWHAE status
BTF3 status
CXCR6
YWHAE
BTF3
Sex
TMB (Z−score)
Metastatic site
Gene expression (Z−score)
Clinical benefit
CB
ICB
NCB
Objective Response Rate
CRPR
PR
SD
PD
Status
High
Low
Sex
F
M
TMB (Z−score)
Metastatic site
Adrenal
Liver
LYMPH NODES
OTHER
SKIN/SOFT TISSUE
SoftTissue
VISCERAL LUNG
VISCERAL OTHER
I
Cluster TID−G1 TID−G2
Cumulative Progression−Free Survival
p = 1e−04
Time (Months)
Number at risk
Cluster
TID−G1 28 9 3 2 1 1
TID−G2 19 0 0 0 0 0
J
Cluster TID−G1 TID−G2
Cumulative Overall Survival
p = 0.026
Time (Months)
Number at risk
Cluster
TID−G1 28 18 8 4
TID−G2 19 6 2 0

Figure 7

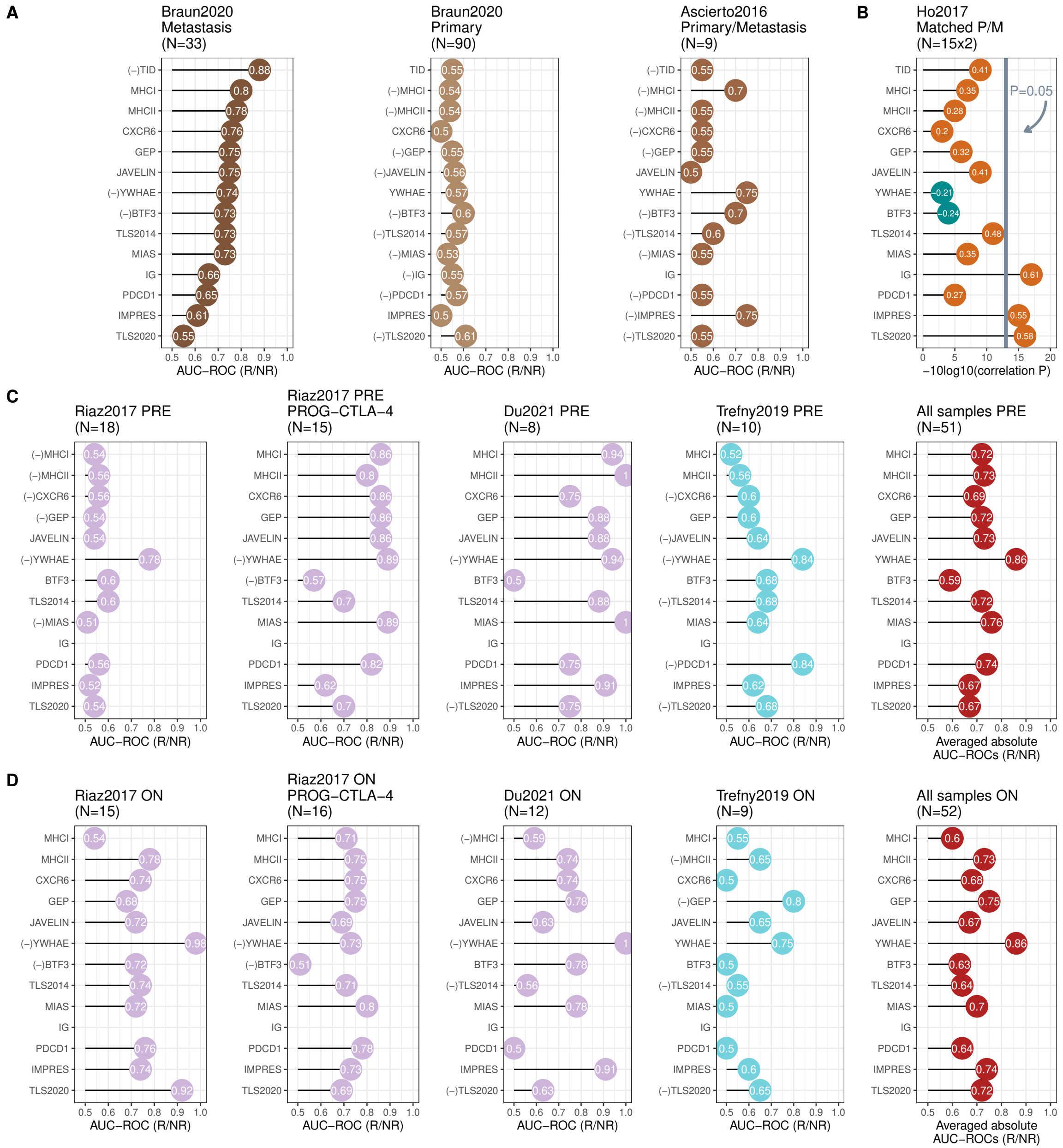
A
Braun2020 Metastasis (N=33)
Braun2020 Primary (N=90)
Ascierto2016 Primary/Metastasis (N=9)
B
Ho2017 Matched P/M (N=15x2)
P=0.05
AUC−ROC (R/NR)
−10log10(correlation P)
C
Riaz2017 PRE (N=18)
Riaz2017 PRE PROG−CTLA−4 (N=15)
Du2021 PRE (N=8)
Trefny2019 PRE (N=10)
All samples PRE (N=51)
Averaged absolute AUC−ROCs (R/NR)
D
Riaz2017 ON (N=15)
Riaz2017 ON PROG−CTLA−4 (N=16)
Du2021 ON (N=12)
Trefny2019 ON (N=9)
All samples ON (N=52)
TID
(−)TID
MHCI
(−)MHCI
MHCII
(−)MHCII
CXCR6
(−)CXCR6
GEP
(−)GEP
JAVELIN
(−)JAVELIN
YWHAE
(−)YWHAE
BTF3
(−)BTF3
TLS2014
(−)TLS2014
MIAS
(−)MIAS
IG
(−)IG
PDCD1
(−)PDCD1
IMPRES
(−)IMPRES
TLS2020
(−)TLS2020